MEASUREMENT OF HARMONICS IN A UNDERDENSE CO_2 LASER PRODUCED PLASMA

by

YUEQIANG ZHU

B.A.Sc. N.W. Telecommun. Eng. Institute 1982

Xian, People's Republic of China

A THESIS SUBMITTED IN PARTIAL FULFILMENT OF

THE REQUIREMENTS FOR THE DEGREE OF

MASTER OF SCIENCE

in

THE FACULTY OF GRADUATE STUDIES

(DEPARTMENT OF PHYSICS)

We accept this thesis as conforming

to the required standard

THE UNIVERSITY OF BRITISH COLUMBIA

September 1986

©Yueqiang Zhu

In presenting this thesis in partial fulfilment of the requirements for an advanced degree at the University of British Columbia, I agree that the Library shall make it freely available for reference and study. I further agree that permission for extensive copying of this thesis for scholarly purposes may be granted by the head of my department or by his or her representatives. It is understood that copying or publication of this thesis for financial gain shall not be allowed without my written permission.

Department of Physics

The University of British Columbia
1956 Main Mall
Vancouver, Canada
V6T 1Y3

Date Nov. 13, 1986

ABSTRACT

Second harmonic($2\omega_0$) and three halves harmonic($3/2\omega_0$) are studied in the interaction of CO_2 laser of frequency ω_0, with an underdense plasma. It is shown theoretically that filamentation can lead to sizable second harmonic generation. The $2\omega_0$-radiation is emitted into a forward directed cone, its angle determined by the wavelength of the fundamental radiation in the plasma filament. Experimental observations confirm the theoretical predications. Aside from the forward directed emission cone, non negligable $2\omega_0$ power is detected over a broad angular range in the backward direction showing a broadened red shifted spectrum. The dependence of the backward emitted $2\omega_0$-radiation on the plasma density, and the red shifted spectrum strongly support the argument that the backward emitted $2\omega_0$-radiation is related to the SBS(Stimulated Brillouin scattering) instability. Based on the wave vector matching conditions, the angular distribution of $3/2\omega_0$-radiation is predicted. The experimental results confirm the prediction. It is shown experimentally that the fusion of three plasma waves produced in the TPD(Two Plasma Decay) instability dominates the generation of $3/2\omega_0$-radiation when the incident beam energy is high.

TABLE OF CONTENTS

LIST OF FIGURES

ACKNOWLEDGMENTS

I would like to thank my supervisor, Dr. Jochen Meyer, for his support and guidance during the course of the project. I also like to thank Grant McIntosh and J.E. Bernard for their helpful suggestions and conversations. Special thanks are extended to Hubert Houtman, Al Cheuck, and Jack Bosma for all their help.

CHAPTER 1

INTRODUCTION

Since the development of high power lasers, entirely new fields of physics have opened up. The heating, evaporation and ionization of matter by laser energy have offered new techniques. Research on plasma entered regions where much higher densities, temperatures, and pressures were encountered than before. Many nonlinear optical effects in the laser-plasma interactions are then easily observable. These nonlinear effects in fact are hardly avoidable in laser heating of plasma and in laser-induced fusion work. The development of high power lasers gives a reasonable hope of success for heating laser-produced plasma up to condition of nuclear fusion. Consequently, the study of nonlinear optical effects in plasmas has become one of most active research fields in plasma physics.

A plasma is a highly nonlinear optical medium. Therefore there are various nonlinear optical effects, such as parametric decay or oscillating two-stream(OTS), two-plasmon decay(TPD), stimulated Raman scattering(SRS), stimulated Brillouin scattering(SBS), harmonic generation, filamentation, and nonlinear effects, such as high energy electron generation. Understanding these nonlinear effects in plasma is important and essential since they have a direct influence on the laser heating of plasma and are the worst problems in the coupling of the laser energy to the target in proposed laser fusion schemes [1]. TPD and SRS, for example, may create very energetic electrons, which can preheat the target core; SBS can prevent some of the incident beam energy from being absorbed in the plasma; filamentation can affect the illumination symmetry.

The study of nonlinear effects in the interaction between a laser and a laser-produced plasma is an ongoing project in this laboratory. SBS and SRS were thoroughly studied by J.E. Bernard[2] and G. McIntosh [3] respectively in the interaction of an intense CO_2 laser beam with a laser-produced subcritical density gas jet plasma. High energy electron generation are being studied by L. Legault[4]. TPD has been studied for a long time [5-8]. My study is the second harmonic generation and $(3/2)\omega_0$(ω_0 is the incident laser beam frequency.) harmonic generation. The original aim of my study is to obtain quantatitive information about $(3/2)\omega_0$ and to understand the properties of $(3/2)\omega_0$, as well as to obtain the correlation between $(3/2)\omega_0$-radiation and TPD instability since it is generally believed that the generation of $(3/2)\omega_0$-radiation is due to the TPD instability. During the measurements, we accidently found $2\omega_0$ in the interaction. This was not reported by other people in an underdense plasma interaction before. Generally it is believed that there will be no second harmonic radiation generated in the interaction of a laser beam with a plasma in which there is no critical density layer. Hence, the observation of second harmonic radiation in our measurement raised several questions: 1) Is our plasma really a underdense plasma without a critical density layer? 2) If the plasma is underdense, what is the mechanism for creation of second harmonic radiation? These two questions are very important and interesting for us, therefore we put much effort into the measurement of second harmonic radiation.

Through the measurement of angular distribution, spectra, dependence on the polarization of the incident beam and on the target density and target material, and the correlation with other nonlinear effects, of second harmonic radiation and three halves harmonic radiation, we try to understand their properties and find the mechanisms for the generation of $2\omega_0$ and $(3/2)\omega_0$ experimentally.

This thesis is organized in the following way. In Chapter 2 we give the theoretical predications about the angular distribution, spectrum of $(3/2)\omega_0$ and a

self-consistent theory for $2\omega_0$-radiation. Although the generation of second harmonic in underdense plasma is a new phenomenon, three halves harmonic has been studied theoretically and experimentally in underdense plasma with either a solid target or a gas target for a long time. The accidental discovery of $2\omega_0$ in underdense plasma was a result of the improvement of the original experimental arrangement. Chapter 3 gives the details about the original experimental setup and the final arrangement. Our experimental results are presented in Chapter 4. Our experimental results, in some aspects, do not agree with the theoretical predication. Chapter 5 gives the detailed discussion about our results. The summary of our original contributions and the conclusion of our experiment are given in the last chapter. In the last chapter several suggestions for the future work are proposed.

CHAPTER 2

THEORY

In the interaction of laser radiation with inhomogeneous, underdense plasmas, as mentioned in previous chapter, a number of parametric instabilities, as well many nonlinear optical processes can occur. However each instability or nonlinear process can only occur if certain conditions are satisfied and the intensity of the incident beam exceeds the threshold. Section 1 gives the general physical conditions and matching conditions for the three-wave processes in laser-plasma interactions. The general mechanism of $(3/2)\omega_0$ generation and the theoretical predictions about $(3/2)\omega_0$-harmonic angular distribution and spectrum are described in Section 2. In Section 3 we discusse the second harmonic generation in an underdense plasma and calculate the $2\omega_0$ intensity distribution emitted from a Gaussian beam.

2.1 Physical Picture for the Nonlinear Processes

When a laser beam is incident on an initially solid target or gas target, a plasma is rapidly formed on the front surface of the target, thereafter the laser beam interacts with the plasma. Because a plasma is a nonlinear medium, many nonlinear optical processes occur in the interaction. The propagation of the laser beam is modified by the plasma: the incident beam is reflected, scattered, or refracted. The dispersion relation for laser radiation in a plasma is:

$$k_0^2 c^2 = \omega_0^2 - \omega_p^2 \qquad (2-1)$$

where k_0 and ω_0 are the wave number and frequency of the laser beam, and $\omega_p = \left(\frac{e^2 n_e}{\varepsilon_0 m_e}\right)^{1/2}$ is the plasma frequency and is proportional to the square root of the plasma density n_e. Thus, as the laser beam propagates into the inhomogeneous plasma from lower density edge to high density layer, its wave number gets smaller and smaller. Finally, at the critical density $n_c = \frac{m_e \varepsilon_0 \omega_0^2}{e^2}$, where the wave number is zero, the laser beam can no longer propagate. From eq.(2-1), one can see that as $n_e > n_c$, the wave number becomes imaginary, and the laser beam decays exponentially(e^{-kx}). Therefore the critical density layer is the classical reflection surface for a laser beam of frequency ω_0 at normal incidence (laser beam incident on a plasma density gradient at an angle θ to the normal, the classical reflecting point for the laser beam occurs at a density $n_e(\theta) = n_c \cos^2\theta$)[9].

Since the laser beam cannot penetrate to the region where the plasma density n_e is above n_c, all laser beam absorption and nonlinear processes occur in the underdense plasma region where the plasma density $n_e < n_c$. It is believed that three kinds of waves can be supported by a inhomogeneous underdense plasma: electromagnetic wave(E_0), electron plasma wave (E_p), and ion acoustic plasma wave (I_p). The electron plasma wave and ion plasma wave have the respective approximate dispersion relations[2]:

$$E_p: \quad \omega^2 = \omega_p^2 + \frac{3k_B T_e}{m_e} k^2 \qquad (2-2)$$

$$I_p: \quad \omega^2 = \frac{Z k_B T_e + 3k_B T_i}{m_i} k^2 \qquad (2-3)$$

where k_B is Boltzmann's constant, $T_e(T_i)$ is the electron (ion) temperature, $m_e(m_i)$ is the electron (ion) mass, Z is the number of the unit charge on the ion. Since there are three plasma modes one could, in principle, find six kinds of interaction modes in the plasma:

(1) $E_0 \rightarrow E_p + E_0'$ (SRS)

(2) $E_0 \rightarrow I_p + E_0'$ (SBS)

(3) $E_0 \rightarrow E_{p1} + E_{p2}$ (TPD)

(4) $E_0 \rightarrow E_p + I_p$ (Parametric Decay)

(5) $E_0 \rightarrow I_{p1} + I_{p2}$

(6) $E_0 \rightarrow E_{01} + E_{02}$

In addition, each interaction mode has to satisfy the wave vector and frequency matching conditions or momentum and energy conditions (also called Manley–Rowe relations[10]):

$$\vec{k}_0 = \vec{k}_1 + \vec{k}_2 \qquad (2-4)$$

$$\omega_0 = \omega_1 + \omega_2 \qquad (2-5)$$

and its own dispersion relation relating ω and k. Then we find that the interaction mode(5) and (6) are impossible in the plasma as they cannot fulfill the matching conditions and the dispersion relations simultaneously. The two ion wave restrictions of the mode (5) should be obvious as these are by definition low frequency modes. The two EM wave case is not as obvious and next we prove that in the mode (6) the matching conditions and dispersion relation cannot be satisfied simultaneously.

First we assume that in the mode (6), the matching conditions can be satisfied. Then subsitituting eq. (2–4) and (2–5) into eq. (2–1), we get:

$$2\omega_1\omega_2 = 2c^2\mathbf{k}_1 \cdot \mathbf{k}_2 - \omega_p^2. \qquad (2-6)$$

From eq. (2–1) we know that :

$$\omega_1 = \sqrt{k_1^2c^2 + \omega_p^2} > k_1c, \qquad (2-7)$$

$$\omega_2 = \sqrt{k_2^2c^2 + \omega_p^2} > k_2c. \qquad (2-8)$$

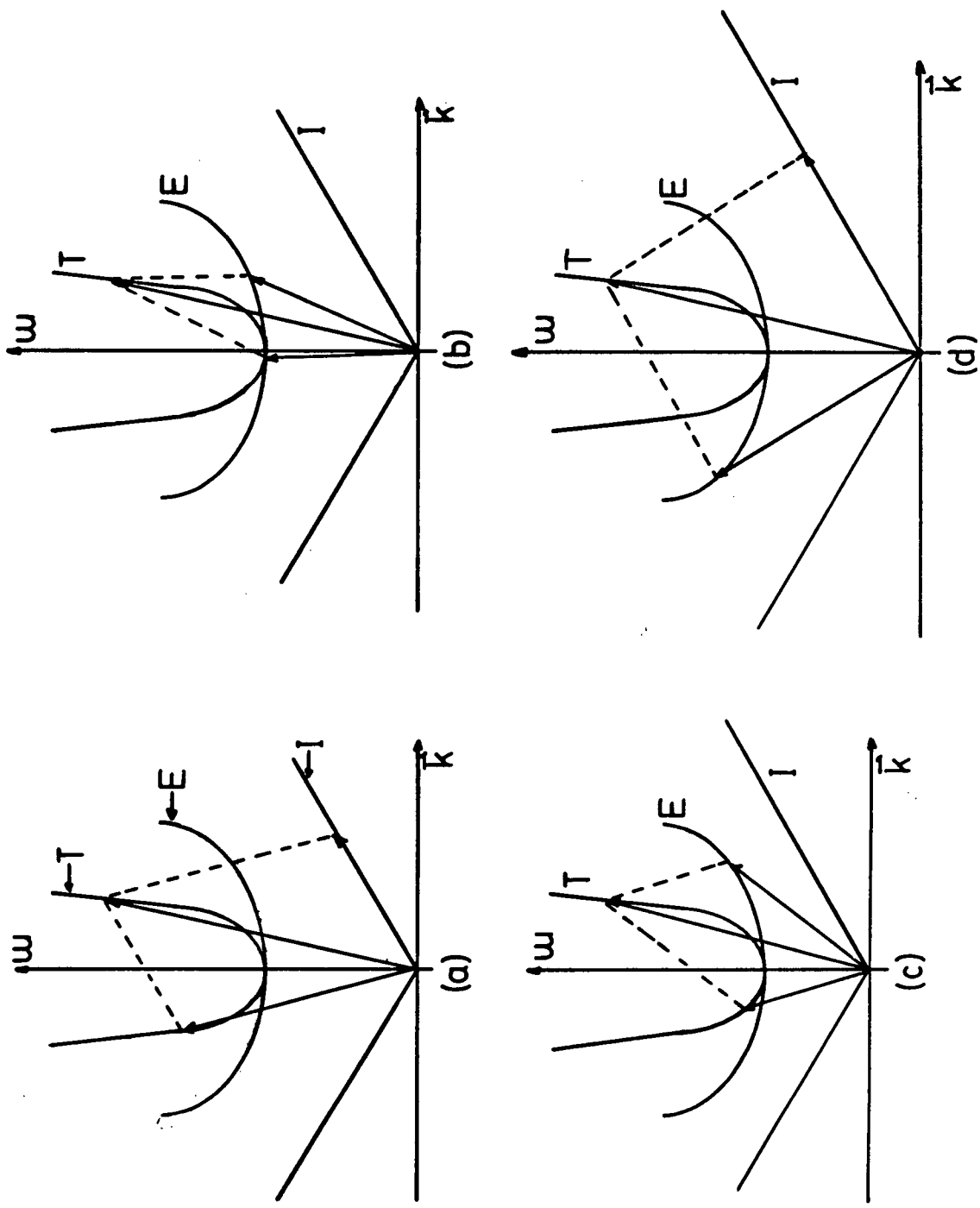

Figure 2-1 Plots of ω vs $\vec{k}$ for three wave processes in an inhomogeneous plasma. (a) SBS, (b) TPD, (c) SRS, (d) Parametric decay. Here I stands for Ion-acoustic plasma wave, E for Electron plasma wave, and T for Transverse E.M wave.

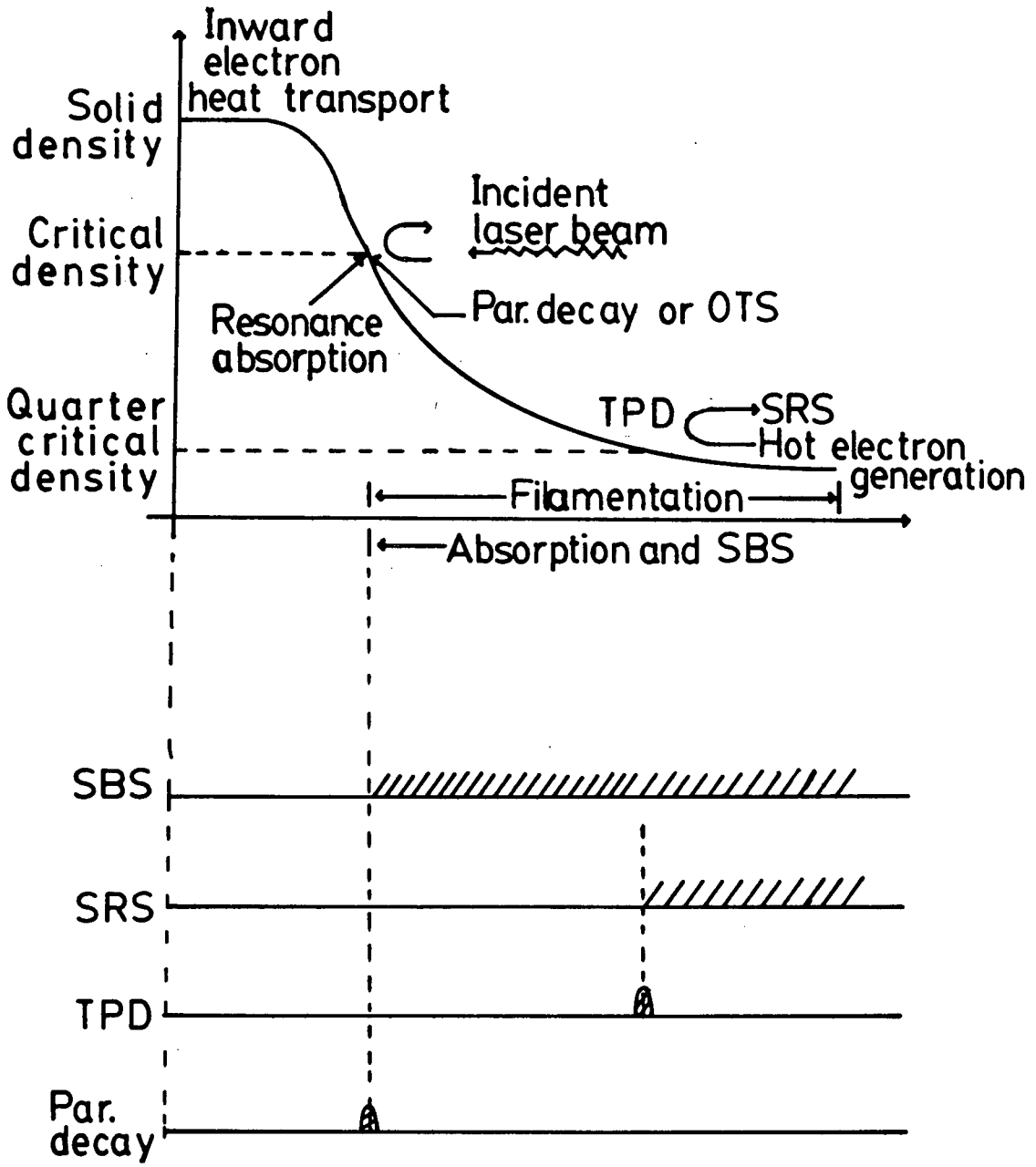

Figure 2-2 Schematic picture. The picture of plasma density profile in a laser produced plasma, showing location of major nonlinear processes in laser-plasma interaction

In addition $\mathbf{k}_1 \cdot \mathbf{k}_2 < k_1 k_2$, thus:

$$2\omega_1\omega_2 > 2c^2\mathbf{k}_1 \cdot \mathbf{k}_2 - \omega_p^2. \qquad (2-9)$$

We see eq. (2-9) is contrary to eq. (2-6). Therefore our assumptoin is not true and in the mode (6), the matching conditions and the dispersion relation cannot be satisfied simltaneously.

Hence, there are four types of three-wave processes which can occur in the plasma as shown in Fig.2-1 where T stands for the incident beam, E for an electron plasma wave, and I for an ion-acoustic wave. In Fig.2-1, each curve is plotted according to the dispersion relation in one dimension. On the other hand, the dispersion relations involve the plasma frequency which is related to the plasma densities, therefore each of the three-wave processes can only occur in some special density region. Fig. 2-2 shows schematically the regions where the above three-wave processes and other nonlinear processes occur in an inhomogeneous underdense plasma [9].

2.2 Theoretical Results on $(3/2)\omega_0$ Generation

From Fig.2-2, one can find that TPD instability can only occur in the plasma region where the plasma density n_e is around quarter critical density. The occurrence of the TPD instability is commonly inferred indirectly in laser-plasma interaction experiments by either the production of energetic clectrons[11,12,13] or by the emission of light at $(3/2)\omega_0$ [14-21], or measured directly by Thomson scattering[22,7]. In addition, it is generally believed that the splitting of the $(3/2)\omega_0$ spectrum has possible application as a coronal temperature diagnostic. Hence much attention has been given to the $(3/2)\omega_0$ studies, and several theories and models have been built[23-25], and a lot of experiments have been done about the $(3/2)\omega_0$ harmonic[16,22,23,26-31].

It is widely accepted that the $(3/2)\omega_0$ harmonic can be generated by two mechanisms, both involving plasma waves of frequency $\omega_0/2$ which are produced in TPD instability. The first is the coupling of the incident $(\vec{k}_0, \omega_0)$ laser beam, or reflected $(-\vec{k}_0, \omega_0)$ laser beam which is due to the SBS instability in underdense plasma, with $\omega_0/2$ plasma wave, and the second is the fusion of three $\omega_0/2$ plasma waves. We can see that these two mechanisms belong to different order nonlinear processes, the first is the second order nonlinear process and the second is the third order one. Generally speaking, the higher order nonlinear process is thought to be much weaker than lower order one. Hence, the first mechanism is commonly thought to dominate the generation of $(3/2)\omega_0$ emission [26], but Avrov et al. [24] predicts that the second can be a dominant mechanism in a number of practically interesting cases, where the probability of a three wave process is low as a result of the nonfulfillment of the wave vector matching conditions with respect to the wavelengths, and Barr [32] predicts that both mechanisms will generate similar spectra. In this section we give the results of the different theories about $(3/2)\omega_0$ angular distribution and spectrum. The detailed theories about $(3/2)\omega_0$ harmonic can be found elsewhere[23-25].

2.2.1 Angular distribution

Using the wave equation for the scattered radiation from Liu and Rosenbluth, namely,

$$\left(c^2\nabla^2 - \frac{\partial^2}{\partial t^2} - \omega_p^2(x)\right) E_s = E_0\omega_p^2 \frac{\delta n}{n}(\vec{e}_0 \cdot \vec{e}_p).$$

where E_0 and E_s are the electric fields of the electromagnetic (EM) waves, and $\vec{e}_0$ and $\vec{e}_p$ are unit vectors for the electric field direction of the incident EM waves and the plasma wave, and taking a WKB approximation and the saturated $\frac{\delta n}{n}$ values, Karttunen[33] calculated reflectivity of $(3/2)\omega_0$-radiation due to the first mechanism

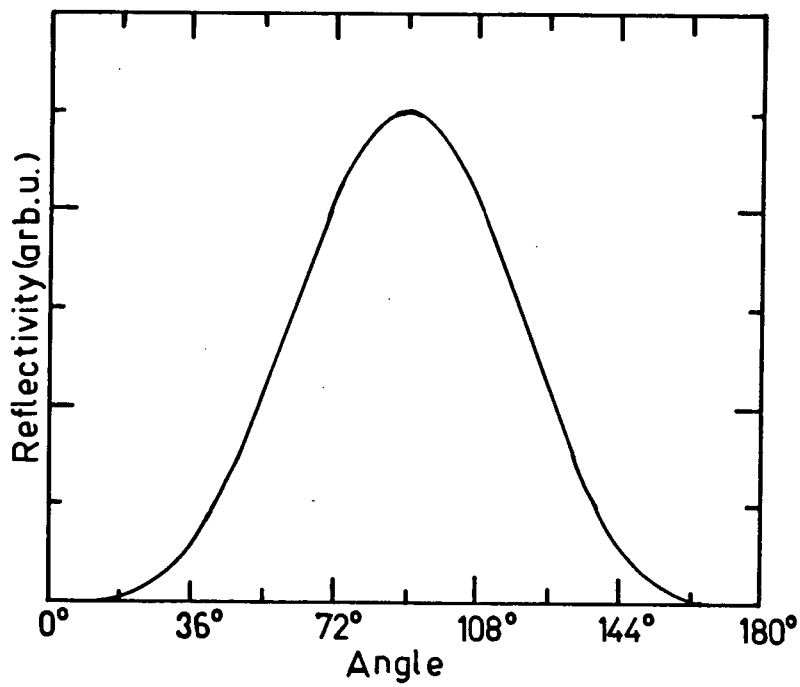

Figure 2-3 $(3/2)\omega_0$ reflectivity from the theory of Karttunen with arbitrary vertical scale.

as shown in Fig. 2-3. We see $I_{(3/2)\omega_0}$ peaks in the normal direction to the incident beam, and has minimum values in backward and forward directions.

Although Avrov et al. used different equations to analyse the generation of $(3/2)\omega_0$ harmonic for both mechanisms[24], the equation of nonlinear interaction of plasma oscillations, but they got the same result for the $(3/2)\omega_0$ harmonic angular distribution as that Karttunen got: the most intense emission of $(3/2)\omega_0$ harmonic occurs at an angle $\theta \sim \pi/2$ with respect to the heating laser beam. Recent experimental result[22] does not agree with these predictions. The $(3/2)\omega_0$ harmonic intensity not only peaks in the normal direction, but also in the backwards direction.

In addition, both the theoretical results and experimental results are not consistent with the result obtained from the matching conditions.

Considering the wave number spectrum of plasma waves, we can get two possible configurations for the generation of $(3/2)\omega_0$ harmonic as shown in Fig. 2-4. In the first, the incident beam is scattered directly by a plasma wave; in the second, the incident laser beam is first reflected by ion plasma waves generated by a SBS instability in the underdense plasma, and the reflected incident beam is then scattered by another plasma wave. Using EM wave dispersion relation eq. (2-1) and taking $\omega_p \approx \omega_0/2$ at quarter critical plasma density region, we can describe k_0 and k_s in terms of ω_0:

$$k_0 = \frac{\sqrt{3}}{2}\frac{\omega_0}{c}$$

$$k_s = (\frac{8}{3})^{1/2} k_0.$$

Since for a given scattering angle θ, only one plasma wave can satisfy the resonant k-matching condition, the amplitudes of the plasma wave and the k-matching condition can determine the angular distribution of $(3/2)\omega_0$ emission when the incident beam intensity is above the threshold of the TPD instability.

In the TPD instability, the plasma waves having largest amplitude are two waves which propagate in opposite directions and lie in the plane of $\mathbf{E}_0$ and k_0 (i.e. the plane of the polarization of the incident beam) at angle $\sim 45°$ with respect to these vectors as shown in Fig. 2-5[2]. From ref. 2 and 7 we know that the plasma waves produced in the TPD instability have maximum growth rate at $\sim 45°$ and $\sim 135°$ and $k_p/k_0 \geq 1.8$ As $k_p = 1.9k_0$ at 135°, the wave vector matching condition and frequency matching conditions for scattering of the incident CO_2-laser light into $\theta = 109°$ are satisfied. Hence $(3/2)\omega_0$-emission should peak at $\theta = 109°$. Similarly, the reflected incident beam causes another peak of $(3/2)\omega_0$ emission in $\theta = 180° - 109° = 71°$. Since the forward incident beam is stronger than back-scattering due to SBS, we expect the peak of $(3/2)\omega_0$ emission at 109°is stronger than that

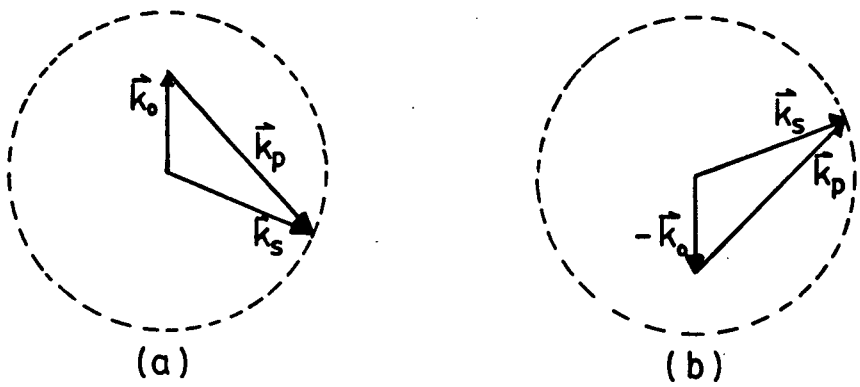

Figure 2-4 The $\vec{k}$-diagrams of the Raman scattering processes for the generation of $(3/2)\omega_0$-radiation(k_s). (a)incident beam is scattered by plasma waves; (b) reflected incident beam is scattered by plasma waves.

at 71°. This angular distribution of $(3/2)\omega_0$ emission based on matching conditions is different from the theoretical results in ref. 24, 33 and the experimental results obtained in the interaction of CO_2 laser with an underdense preformed plasma with a relatively long density scale length(similar to our experimental setup) in ref. 22. We will compare these theoretical predictions and experimental results with our experimental result in Chapter 5.

So far, with the matching conditions we have analyzed the angular distribution due to the first mechanism, the coupling of the incident beam with a $\omega_0/2$-plasma wave produced in the TPD instability. Next with the matching condition we analyze the angular distribution due to the second mechanism, the fusion of three plasma waves produced in the TPD instability.

As mentioned in the previous paragraph, Avrov et al. thought that the second mechanism can dominate the generation of $(3/2)\omega_0$-radiation as the probability of the first mechanism is lower as the result of the nonfulfillment of the wave vector matching condition for the resonance with respect to the wavelength. From ref. 7,

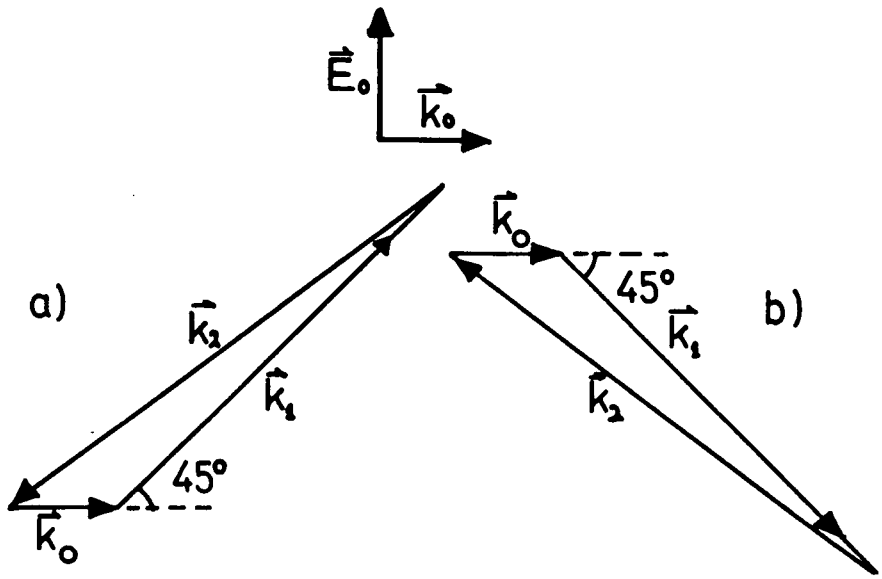

Figure 2-5 A $\vec{k}$-diagram for TPD . The electron plasma waves lie in the plane containing both $\mathbf{E}_0$ and $\mathbf{k}_0$. a) and b) show the two strongest pairs of electron plasma waves.

we see, $k_p = 1.9k_0$, which can satisfy the wave vector matching condition for the first mechanism, scattering of the incident beam into $\theta = 109°$ at $(3/2)\omega_0$, is just at the lower limit of the detectable plasma wave in TPD instability and most of plasma waves with larger wave vector cannot satisfy the wave vector matching condition for the first mechanism. The wave vector matching condition can be satisfied easily in the fusion of three plasma waves produced in TPD instability because of the very wide wave vector spectrum of the plasma waves. For simplicity, we consider that two plasma waves with frequency, $\omega_0/2$ in the same direction interact with the third $\omega_0/2$-plasma wave in the opposite direction to generate the $(3/2)\omega_0$-radiation

emitted in the same direction as that of the first two plasma waves. As shown in Fig. 2-5, when $k_1 = 1.8k_0$ and $\vec{k}_1$ is at $\theta = 45°$, $\vec{k}_2$ is at $\theta = 148°$. Since we see most of plasma waves are in the range from $\theta = 135°$ to $\theta = 148°(\bar{\theta} \doteq 142°)$ and the range from $\theta = 32°$ to $\theta = 45°(\bar{\theta} \doteq 39°)$, we should also see the $(3/2)\omega_0$-radiation generated by the fusion of three plasma waves in the same directions. Considering the effect of the reflection of the forward emitted $(3/2)\omega_0$-radiation due to SBS instability, the backward emitted $(3/2)\omega_0$-radiation should be a little stronger than the forward emitted $(3/2)\omega_0$-radiation.

In summary, based on the matching condition we expect to see four peaks in the angular distribution of the $(3/2)\omega_0$-radiation at $\theta = 71°$ and $\theta = 109°$ due to the first mechanism, and at $\theta = 39°$ and $\theta = 142°$ due to the second mechanism; the peak in the backward direction is stronger than that in the forward direction in both mechansims, and peaks due to the first mechanism are stronger than those due to the second mechanism since the first mechanism is one order lower nonlinear process than the second mechanism. It is expected that the $(3/2)\omega_0$-radiation intensity does depend on the incident beam polarization since most of the plasma waves produced in the TPD instability lie in the plane of polarization of the incident beam.

2.2.2 Spectrum of $(3/2)\omega_0$

In TPD instability, the plasma wave frequencies $\omega_{1,2}$ are both approximately equal to ω_p. Then eq. (2-2) can be simplified as:

$$k_{1,2} = \frac{1}{v_e}[\frac{2}{3}\omega_p(\omega_{1,2} - \omega_p)]^{1/2}. \qquad (2-10)$$

Here v_e is electron thermal velocity. Thus we see the TPD instability will occur as $\omega_p \leq \omega_{1,2}$.

Considering the two mechanisms of $(3/2)\omega_0$ emission, Avrov et al. [24] obtained two different frequency shifts for $(3/2)\omega_0$ emission in different processes,

respectively:

$$\delta\omega_{3/2}^{\ell t} \doteq 4.6 \times 10^{-3} T_e \omega_0 \mid \cos\theta \mid \qquad (2-11)$$

$$\delta\omega_{3/2}^{3\ell} \doteq 4.8 \times 10^{-3} T_e \omega_0 \cos\theta \qquad (2-12)$$

where $\delta\omega_{3/2}^{\ell t}$ is the frequency shift from $(3/2)\omega_0$ in the $(3/2)\omega_0$-radiation spectrum for the first mechanism, coupling of the incident beam with a plasma wave produced in TPD; $\delta\omega_{3/2}^{3\ell}$ is the frequency shift in the spectrum in the second mechanism, fusion of three plasma waves produced in TPD. From eq. (2–11), we see the spectrum of $(3/2)\omega_0$-radiation due to the first mechanism has blue shift in all directions. While from eq. (2–12), we see the spectrum of $(3/2)\omega_0$-radiation due to the second mechanism has blue shift in the forward directions and red shift in the backward directions. Thus with eq. (2-11) and (2-12) we can relate the observed $(3/2)\omega_0$ emission frequency shifts with the plasma temperature in the plasma region of $(1/4)n_c$.

Using the parameters of our system, we can make a numerical estimate about the wavelength shift of $(3/2)\omega_0$-radiation from $(2/3)\lambda_0$. Subsitituting $T_e = 0.3\text{keV}$, $\theta = 144°$, and $\lambda_0 = 10.6\mu m$ into eq. (2-11), we get $\triangle\lambda = -5.3nm$, and into eq. (2-12) we get $\triangle\lambda = 5.5nm$.

2.3 Theoretical Consideration of Second Harmonic Generation

Significant harmonic frequency generation in dense laser produced plasma has been observed in the past[35–37] and is generally associated with the anharmonic oscillation of resonantly excited electrons in a steep density profile. More recently second harmonic $(2\omega_0)$ generation has been associated with filamentation[38]. In this case $2\omega_0$ -radiation was shown to be emitted from filamentary structures in the underdense target corona in direction perpendicular to the laser beam. The theoretical analysis required the presence of incident and backscattered waves at frequencies$\sim \omega_0$ in the filament[38].

The question arises whether $2\omega_0$ -emission from plasmas, of densites n_e lower than the critical density, n_c is always associated with self focussing and whether certain signatures of the $2\omega_0$ radiation then permit conclusions to be drawn about the generating filaments. If this were possible, one might consider the study of $2\omega_0$ -emission from underdense plasmas, such as those generated by exploding foils, in order to assess the potential dangers of the filamentation instability for actual compression experiments.

Our studies about $2\omega_0$ attempt to address these questions. In this section we discuss the second harmonic generation in an underdense plasma and calculate the $2\omega_0$ intensity distribution emitted from a Gaussian beam. In Subsection 1, we consider the case of a single electron, immersed in an E.M field with frequency ω_0. It is shown that the electron emits radiation with frequency $2\omega_0$ as a results of the nonlinear effects. Then, in Subsection 2 we extend the results to the case with many electrons by taking account of the relative phases and amplitudes of the scattering wave.

2.3.1 Single Electron

We start the discussion with the equation of the motion for an electron:

$$m_e \frac{d\mathbf{v}}{dt} = -e(\mathbf{E} + \mathbf{v} \times \mathbf{B}) \qquad (2-13)$$

where m_e is electron mass, $-e$ is electron charge. Every variable in eq. (2-13) is written as:

$$\mathbf{A} = \mathbf{A}_0 + \varepsilon \mathbf{A}_1 + \varepsilon^2 \mathbf{A}_2 + \cdots\cdots \qquad (2-14)$$

where $\frac{A_n}{A_0} = 0(1)$, and $\varepsilon = \frac{eE_0}{m_e \omega c} = \frac{v_q}{c} \ll 1$, v_q is the quiver velocity produced in the electron by $\mathbf{E}_0$ of the laser beam. For a cold plasma, $\frac{|\mathbf{v}\times\mathbf{B}|}{|\mathbf{E}|} = \frac{v}{c} \ll 1$. The only nonlinear term is the Lorentz force term in eq. (2-13) and it is much weaker than the Coulomb force term. As we consider $\varepsilon = \frac{eE_0}{m_e \omega c}$, $\frac{|\mathbf{v}\times\mathbf{B}|}{|\mathbf{E}|} = \frac{v}{c} \to 0(\varepsilon) \ll 1$, and the

plasma has no relativistic velocity, we subsititute the expansion form (2–14) into eq. (2-13) and get a set of nonlinear equations by requiring the coefficient of ε^n to vanish. The two lowest order nonlinear equations are:

$$m_e \frac{d\mathbf{v}_1}{dt} = -e\mathbf{E}_0 \qquad (2-15)$$

$$m_e \frac{d\mathbf{v}_2}{dt} = -e(\mathbf{v}_1 \times \mathbf{B}_0). \qquad (2-16)$$

The Maxwell equations for a uniform plasma(charge density, $\rho = 0$) are of forms:

$$\nabla \cdot \mathbf{E} = 0 \qquad (2-17)$$

$$\nabla \times \mathbf{E} = -\frac{\partial \mathbf{B}}{\partial t} \qquad (2-18)$$

$$\nabla \cdot \mathbf{B} = 0 \qquad (2-19)$$

$$\nabla \times \mathbf{B} = \varepsilon_0 \mu_0 \frac{\partial \mathbf{E}}{\partial t} + \mu_0 \mathbf{J}. \qquad (2-20)$$

Taking each variable in eq. (2-13) as $\mathbf{A} = \mathbf{A}(\mathbf{r})e^{i(\mathbf{k}\cdot\mathbf{r}-\omega_0 t)}$, from eq. (2-18) we can get:

$$\mathbf{B}_0 = -\frac{i}{\omega_0}\nabla \times \mathbf{E}_0, \qquad (2-21)$$

and from eq. (2-15) get:

$$\mathbf{v}_1 = \frac{ie}{m_e \omega_0}\mathbf{E}_0. \qquad (2-22)$$

Subsitituting $\mathbf{v}_1$ and $\mathbf{B}_0$ into eq.(2-16), we get:

$$\frac{d\mathbf{v}_2}{dt} = -\left(\frac{e}{m_e \omega_0}\right)^2 \mathbf{E}_0 \times (\nabla \times \mathbf{E}_0). \qquad (2-23)$$

Since $\mathbf{E}_0 \times (\nabla \times \mathbf{E}_0) = (\mathbf{E}_0 \cdot \nabla)\mathbf{E}_0 + \frac{1}{2}\nabla(\mathbf{E}_0 \cdot \mathbf{E}_0) = \frac{1}{2}\nabla(\mathbf{E}_0 \cdot \mathbf{E}_0)$ as $\nabla \cdot \mathbf{E} = 0$ (this means $\mathbf{k}$ is perpendicular to $\mathbf{E}$ and therefore $(\mathbf{E} \cdot \nabla)\mathbf{E} = 0$), we simply get

the second order ponderomotive acceleration [39] which a single electron of a plasma experiences in the field of an electromagnetic wave:

$$\dot{\mathbf{v}}_2 = -\frac{1}{2}\left(\frac{e}{m_e\omega_0}\right)^2\nabla(\mathbf{E}_0\cdot\mathbf{E}_0). \qquad (2-24)$$

We now consider that the electric field of a focussed laser beam in the interaction region is described in cylindrical coordinates ($\mathbf{r} = \rho, \phi, z$) by:

$$\mathbf{E}(\mathbf{r},t) = \mathbf{E}(\rho)cos(\omega_0 t - kz). \qquad (2-25)$$

Equation (2-24) then contains a longitudinal and a transverse a.c. term which in complex notation are:

$$\dot{v}_z = \frac{1}{2}\left(\frac{e}{m\omega_0}\right)^2 kE^2(\rho)exp[i(2\omega_0 t - 2kz)], \qquad (2-26)$$

$$\dot{v}_t = -\frac{1}{4}\left(\frac{e}{m\omega_0}\right)^2\frac{\partial}{\partial\rho}E^2(\rho)exp[i(2\omega_0 t - 2kz)]. \qquad (2-27)$$

Here $\dot{v}_z$ is the component of $\dot{\mathbf{v}}_2$ perpendicular to $\mathbf{E}$, $\dot{v}_t$ is the component of $\dot{\mathbf{v}}_2$ parallel to $\mathbf{E}$.

The accelerated electron will emit second harmonic radiation which has an electric field at an observer position $\mathbf{r}$, given by[40]:

$$\mathbf{E}^{2\omega_0}(\mathbf{r},t) = -\frac{m}{e}\frac{r_e}{r^3}[\mathbf{r}\times(\mathbf{r}\times\dot{\mathbf{v}}_2)] \qquad (2-28)$$

Here $r_e = e^2/(4\pi\varepsilon_0 mc^2)$ is the classical electron radius. With eq.(2-26) and (2-27):

$$\mathbf{E}_{2\omega_0} = -\frac{1}{2}\frac{e}{m\omega_0^2}\frac{r_e}{r}exp[i(2\omega_0 t - 2kz)]\times[ika E^2(\rho) + \frac{1}{2}b\frac{\partial}{\partial\rho}E^2(\rho)]. \qquad (2-29)$$

Here **a** and **b** in cartesian coordinates(x,y.z) expressed in polar variables (r, Φ, θ) are:

$$\mathbf{a} = (sin\theta cos\theta sin\Phi, sin\theta cos\theta cos\Phi, -sin^2\theta),$$

$$\mathbf{b} = (-cos^2\theta cos\Phi, -cos^2\theta sin\Phi, sin\theta cos\theta).$$

2.3.2 Many Electrons

Before calculating the $2\omega_0$-emission from a plasma we can derive a couple of important conclusions from two simple considerations schematically presented in Fig. 2-6. First we consider the $2\omega_0$-emission from a string of electrons along the incident laser axis oscillating according to eq.(2-26) and (2-27). Positions of maximum oscillation amplitude indicated in Fig. 2-6a are separated by $\lambda_0/2\nu_1$ with ν_1 being the refractive index for the fundamental. An observer at a large distance from the string will only observe $2\omega_0$-radiation at a polar angle θ for which the projected axial separation satisfies the Bragg condition $\lambda_0 \cos\theta/2\nu_1 = \lambda_0/2\nu_2$. Here $\nu_2 (> \nu_1)$ is the refractive index for the second harmonic. Secondly we realize that the exciting laser radiation has a finite cross section and the emission originates from discs of some radius w_o rather than points. Coherent emission from such a disc will occur into an angular diffraction pattern $F(w_o, \theta)$ which is more highly peaked towards $\theta = 0°$ for larger w_o. Combining the two conditions we would expect $2\omega_0$-emission from an underdense plasma into a polar angle θ (determined by the refractive index of the emitting region) at an intensity governed by the diameter of the exciting laser radiation. We will see later that filaments of $w_o \sim \lambda_0$ are required to produce detectable $2\omega_0$ powers.

We now calculate the $2\omega_0$-emission at a distance r from a volume of dimensions $(\ell \ll r)$ with electron density, n_e. Using the Born approximation and cylindrical coordinates (ρ, ϕ, z) we can calculate the resulting field at **r**. Using eq.(2-29) we get:

$$\mathbf{E}_{2\omega_0}(\mathbf{r}, t) = -\frac{1}{2}\frac{e}{m\omega_0^2}\frac{r_e}{r}[ik\mathbf{a}\bar{I}_1 + \frac{1}{2}\mathbf{b}\bar{I}_2] \qquad (2-30)$$

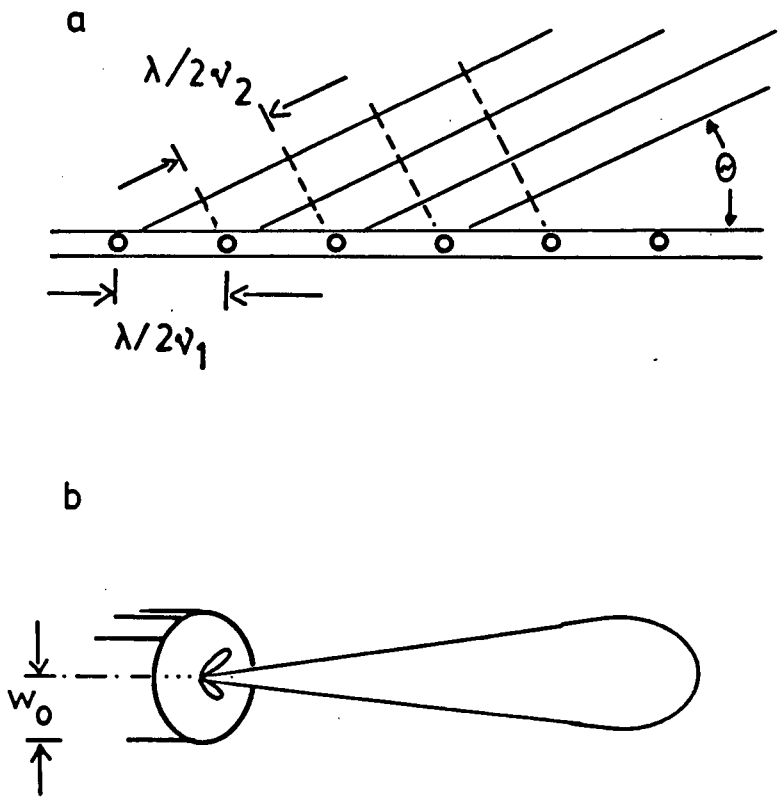

Figure 2-6 Schematic representation of second harmonic radiation. (a) the emission will be directed into an angle θ such that the projected wave fronts are separated by the second harmonic wavelength, (b) the $2\omega_0$ power will be limited by the diffraction pattern of the plasma filament.

with integrals

$$\bar{I}_{1,2} = \int_0^{2\pi} d\phi \int_0^{\infty} \rho d\rho \int_{-\ell/2}^{+\ell/2} dz n_e G_{1,2} \exp[i(2\omega_0 t' - 2kz)] \qquad (2-31).$$

Here $G_1 = E^2(\rho)$ and $G_2 = \frac{\partial}{\partial \rho} E^2(\rho)$. The retarded time t' can be approximated by

$$t' = t - \frac{r}{c_0} + \frac{1}{c_2}(z\cos\theta + \rho \sin\theta \cos\phi).$$

Here c_2 is the phase velocity of $2\omega_0$ light and c_0 speed of light in vacuum. If the length of the volume $\ell \gg \lambda_0$ then the integration over z results in a δ function. Integration over ϕ defines the zero order Bessel function. Writing $c_1 = \omega_0/k$ and $k = \nu k_0$, we obtain from eq. (2-31):

$$\bar{I}_{1,2} = \frac{2\pi^2}{k_0} \exp[i(2\omega_0 t - 2k_0 r)] \times \int_0^\infty \rho d\rho n_e G_{1,2} J_0(2\frac{\omega_0}{c_2}\rho \sin\theta)\delta(1 - \frac{c_1}{c_2}\cos\theta) \qquad (2-31')$$

In order to evaluate the integrals in eq.(2-31') we need to know the functions $n_e(\rho)$ and $E(\rho)$. Here we concentrate on the special cases in which

$$E(\rho) = E_0 \exp(-\rho^2/\mathrm{w}_0^2).$$

$E(\rho)\exp(-i\nu_\mathrm{w} k_0 z)$ describes then either the field in a Gaussian beam waist in a plasma of constant refractive index ν_w or the solution to the wave equation for a parabolic index profile given by $\nu^2 - \nu_\mathrm{w}^2 = 4(1 - \rho^2/\mathrm{w}_0^2)/k_0^2\mathrm{w}_0^2$. In the case of a Gaussian beam waist in a constant density we can take n_0 out of the integrals in eq. (2-31'). For the situation of a parabolic profile we consider the case of zero axial density, in which case $\nu_\mathrm{w}^2 = 1 - 4/(k_0^2\mathrm{w}_0^2)$ and $n_e/n_c = 4\rho^2/k_0^2\mathrm{w}_0^4 \cdot E_0^2(\rho)$ and $n_e(\rho)$ for such a filament is shown in Fig.2-7. The integrals in eq.(2-31') can then be evaluated for both situations with the help of integral tables [41] to obtain $\mathbf{E}_{2\omega_0}(\mathbf{r},t)$. Setting $c_2 \simeq c_0$ for an underdense plasma and using the power $P_0 = \frac{\pi}{2}\varepsilon_0 c_0 \mathrm{w}_0^2 E_0^2$ as well as $\omega_0^2 = e^2 n_c/\varepsilon_0 m_e$ we get:

$$\mathbf{E}_{2\omega_0}(\mathbf{r},t) = -2\pi \frac{P_0}{ec_0}\frac{r_e}{\mathbf{r}}(1 - \nu_\mathrm{w}^2)\exp[i(2\omega_0 t - 2k_0 r)]$$

$$* F_{1,2}(\theta,\phi,x^2)\delta(\nu_\mathrm{w} - \cos\theta). \qquad (2-32)$$

Here, with $x^2 \equiv \frac{1}{2}k_0^2 w^2 \sin^2\theta$,

$$F_1 = \frac{i}{4}a\nu_w e^{-x^2} - \sqrt{\pi}\frac{b}{k_0 w_0}e^{-x^2/2}[(1-x^2)I_0(x^2/2) + x^2 I_1(x^2/2)]$$

for the case of a Gaussian waist in constant density, and

$$F_2 = \frac{i}{4}a\nu_w(1-x^2)e^{-x^2} - \sqrt{2\pi}/32\frac{b}{k_0 w_0}e^{-x^2/2}[3(1-2x^2)I_0(x^2/2)$$

$$+2x^2(2-x^2)I_1(x^2/2)]$$

for the case of a parabolic index profile of axial density $n_0 = 0$. I_0 and I_1 are the zero and first order modified Bessel functions.

Using $a^2 = \sin^2\theta$ and $b^2 = \cos^2\theta$ we can calculate the second harmonic intensity $I_{2\omega_0} = \varepsilon c \mathbf{E}_{2\omega_0} \cdot \mathbf{E}^*_{2\omega_0}$. In an experiment we detect the power passing through some area defined by the acceptance $\triangle\Phi, \triangle\theta$:

$$P_{2\omega_0} = r^2 \int_{\triangle\Phi} d\Phi \int_{\triangle\theta} I_{2\omega_0} \sin\theta d\theta.$$

Since $I_{2\omega_0}$ does not relate to Φ, we integrate $I_{2\omega_0}$ only over θ. After some simple arithmetic we finally obtain for the second harmonic power observed only at θ_0:

$$P_{2\omega_0}(\theta_0) = \frac{\pi}{64}\frac{r_e}{mc_0^3}P_0^2 \triangle\Phi \cos^2\theta_0 \sin^6\theta_0 H_{1,2}(x_0^2) \qquad (2-33)$$

for $\sin^2\theta_0 = 1 - \nu_w^2$. Here

$$H_1(x^2) = 4e^{-2x^2} + 32\pi\frac{e^{-x^2}}{x^2}[(1-x^2)I_0(x^2/2) + x^2 I_1(x^2/2)]^2$$

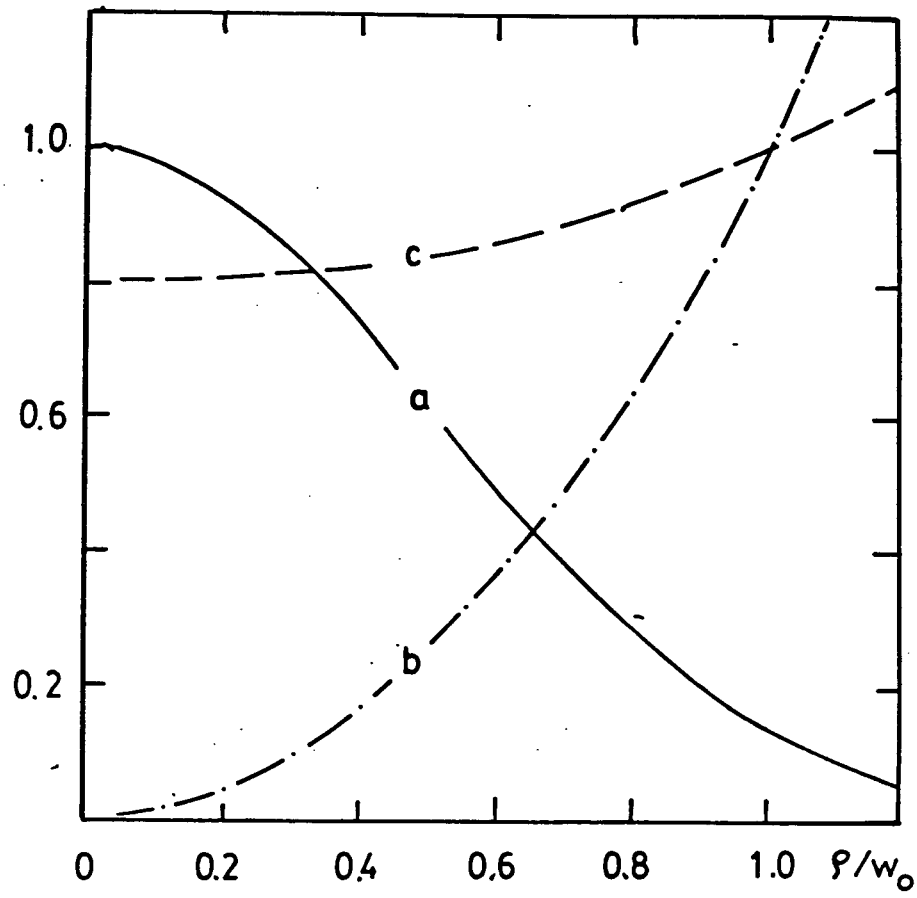

Figure 2-7 Gaussian intensity profile . Curve a: $I(\rho)/I_0$, curve b: $n(\rho)/n_w$ with $n_0 = 0$, and curve c: $n(\rho)/n_w$ with $n_0 = 0.8n_w$.

for a Gaussian waist at constant density, and

$$H_2(x^2) = 2x^2(1-x^2)^2e^{-2x^2} + \frac{\pi}{32}e^{-x^2}[3(1-2x^2)I_0(x^2/2) + 2x^2(2-x^2)I_1(x^2/2)]^2$$

for a parabolic profile with $n_0 = 0$ on the axis.

The function $H_1(x^2)$ and the function $H_2(x^2)$ are shown in Fig. 2-8.

It is instructive to look at some numerical estimates relevant to the experimental investigation described in Chapter 4. We note $\pi r_e/(64mc_0^3) = 5.43 \times 10^{12}W^{-1}$ and in order to detect second harmonic powers in excess of 100 W at $\theta_0 \simeq 27^\circ$ into $\triangle\Phi = 1rad$, we would require $H(x^2) \simeq 10^{-4}$, i.e. $x^2 = 12$ (see Fig. 2-8). In other

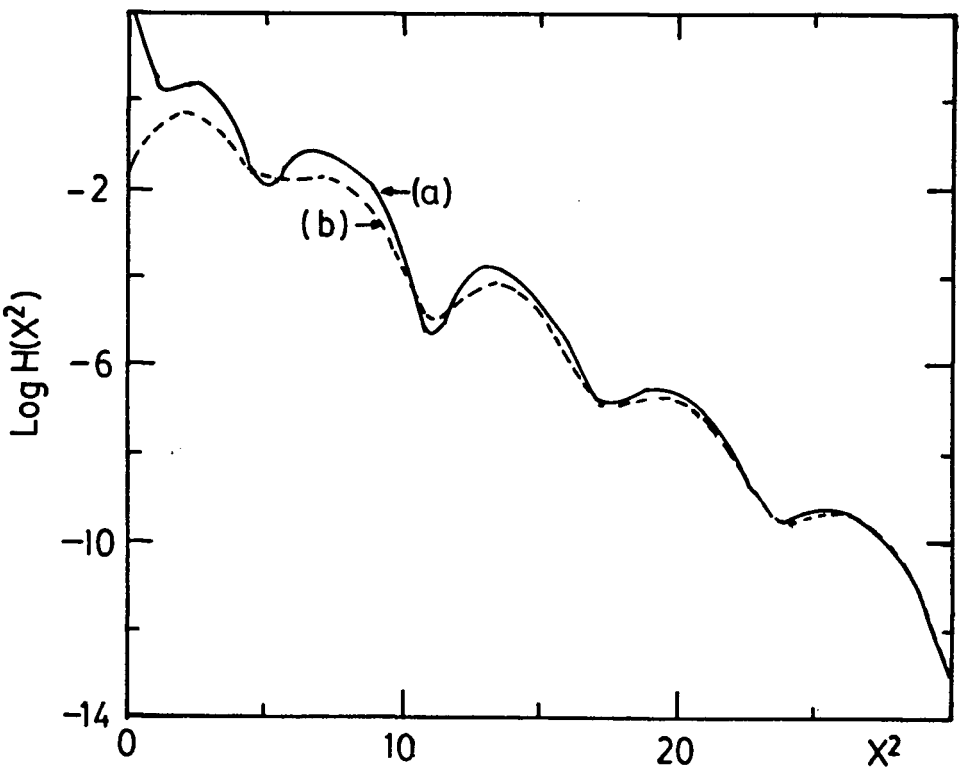

Figure 2-8 The function $H(x^2)$. curve a is for $H1(x^2)$, curve b for $H2(x^2)$.

words, the laser radiation would have to be focussed to a waist of $w_0/\lambda_0 \leq 1.7$. Such tight focus in a plasma arises through the action of the filamentation instability (see e.g. [42]). The general equilibrium of this instability is not amenable to analytic calculations, however studies of a simple slab equibirum[42] and computer simulations (e.g.[38]) show that the radiation modified the dielectric properties of the plasma in such a way to form waves guides. In the limit of very strong fields the instability saturates when the electromagnetic radiation drives all the plasma out of the regions of large field intensity and establishes an equilibrium with radiation inside a vacuum channel surrounded by plasma[43]. Which form this vacuum channel takes or whether the parabolic density profile of the presented calculations provides

a reasonable approximation are questions which cannot be answered analytically. However the results for the second harmonic emission indicating that the $2\omega_0$ radiation is directed into a cone of the angle θ_0 determined by the channel diameter, is proportional to the square of the incident power, and is not related to Φ, i.e. is independent on the incident beam polarization, should be of a more general nature.

The presented analysis neglects the effect of refraction of the second harmonic radiation using the argument that ν for $2\omega_0$ will be very close to one in plasma underdense for ω_0. However if the vacuum channel is deep enough, $2\omega_0$-rays emitted into θ_0 may be trapped in the channel, in which case the present analysis is not correct. The refractive index for $2\omega_0$ can be written $\nu_{2\omega_0}^2 = 1 - \rho^2/k_0^2 w_0^4$. Trapping will set in [45] once θ_0 becomes smaller than a critical angle $\theta_c = \arctan(R/k_0 w_0^2)$, Where R is the maximum channel radius. For $w_0 = \lambda_0$ we have $\theta_0 = 18.6^o$ and in order for $2\omega_0$ trapping to start $R = 2w_0$ is required, i.e. an electron density of n_e/n_c smaller than 0.4. However the present results would only be modified slightly in that now a range of emission angles θ instead of just θ_0 should be expected.

CHAPTER 3

EXPERIMENTAL ARRANGEMENT

As discussed in the last chapter, the generation of $(3/2)\omega_0$ and $2\omega_0$ harmonics greatly depends on the parameters of the CO_2 laser beam and the laser-produced plasma. Section 1 describes our CO_2 laser system and CO_2-laser produced underdense gas jet target plasma and gives their parameters. The experimental arrangements for the measurements of angular distribution and spectrum of $(3/2)\omega_0$ and $2\omega_0$ harmonics are given in Section 2.

3.1 CO_2 Laser System and Plasma

The layout of CO_2 laser and gas jet target is shown in Fig.3-1. Because these system are well known, we only briefly give their main parameters in this section. The detailed description about the system can be found in ref. (45),(46), and (2).

3.1.1 CO_2 laser and gas jet target

A CO_2 laser pulse of 2ns FWHM ($\sim$ 1.2ns rise, 2.8ns fall) with a wavelength $\lambda_0 = 10.6\mu m$ and with an energy of $\leq 12J$ is used to produce and interact with a plasma which is formed in low density nitrogen. The laser beam is focussed onto the target to a $50\mu m(1/e)$ radius by f/7 optics($I_0 \leq 10^{14}W/cm^2$). The target consists of a pulsed, $\sim 1.5mm$ thick nitrogen gas jet which flows from a planar laval nozzle into a stablizing 5 Torr helium background. The focal point of the laser is $\sim 2-4$mm above the jet. The jet has steep density gradients along its edges[17] and a molecular

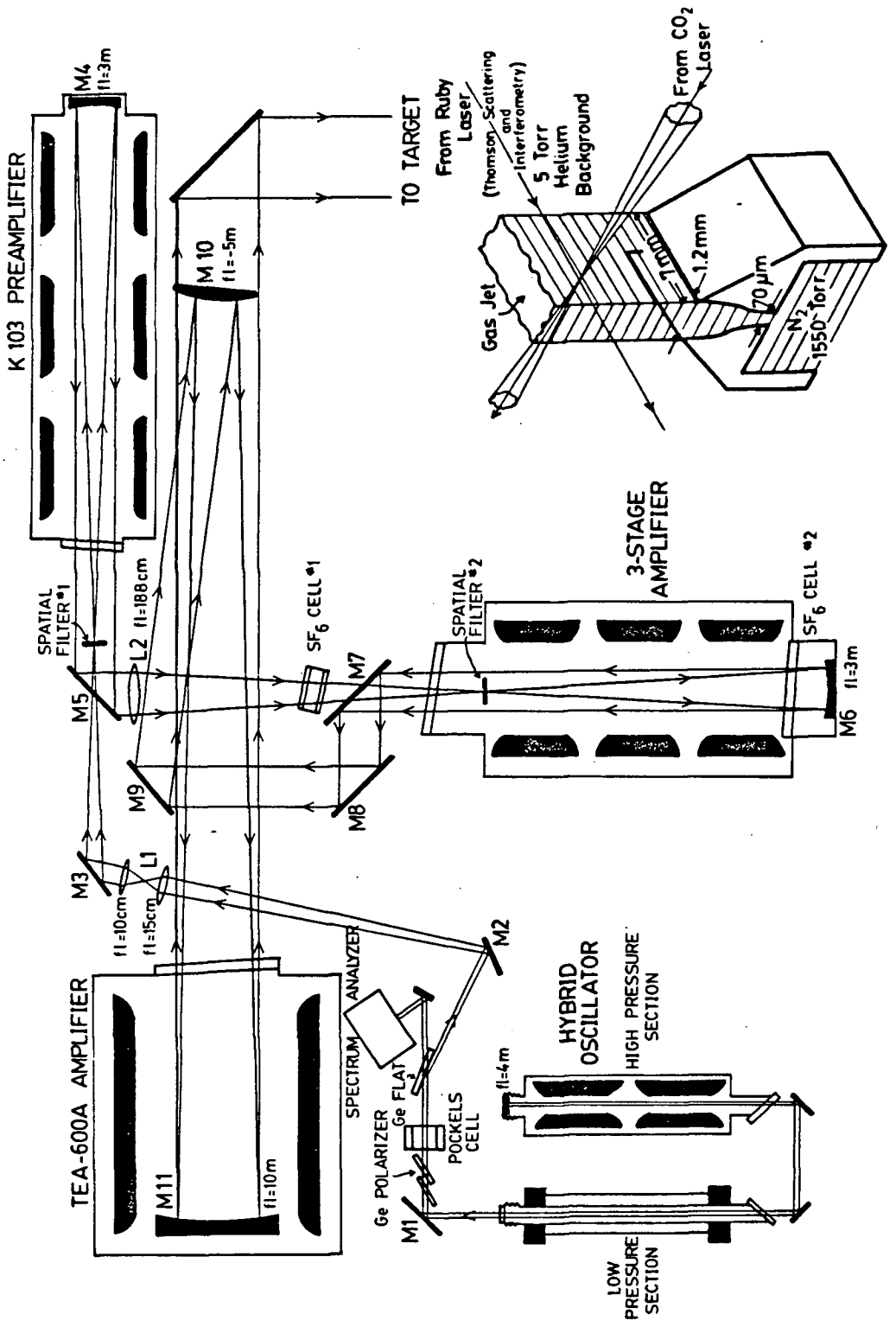

Figure 3-1 Construction of CO_2 laser and gas jet target.

density of $\sim 0.7 \times 10^{18} cm^{-3}$. Approximately 7% of the incident power was reflected from a KCl beam splitter located directly front of the main focussing lens, in order to monitor the incident power.

3.1.2 Plasma

A plasma was produced for all laser energies above $\sim 0.8J$. The plasma first appeared at the front and rear N_2-He interfaces of the jet. Subsequently the development of the rear plasma stopped except for a slow expansion indicating strong refraction or absorption or scattering of the incident light by the front plasma. The plasma at the front jet interface rapidly extended into the background helium. Time resolved ruby laser interferograms revealed a peak plasma density of 0.4 n_c (nitrogen target pressure is 31.5 PSI and heliun backpround pressure is 5 Torr) near the initial plasma location. However the density in front of the jet ranged from $0.05—0.2n_c$ indicating that this plasma was made up of nitrogen and helium ions in the ratio of He:N$\sim$ 1.7. The nitrogen contamination resulted from the $\sim$ 10ms operation of the jet prior to the laser pulse. The average electron temperature during the pulse was measured to be approximately 300eV independent of laser energy and the ion temperature was estimated[47] to be more than an order of magnitude lower.

Unfortunately it is impossible to detect narrow density filaments in Abel unfolded interferograms. However, interferograms taken late in the laser pulse at t=3.3ns and t=3.8ns reveal wider axial density depressions. These can be seen in Fig.3-2.

3.2 Experimental Arrangements

At the beginning, we used the experimental arrangement[2] in which an SF_6 cell was used to absorb the $10.6\mu m$ signal and an IR monochromator was used to separate the harmonics, to measure the $(3/2)\omega_0$-harmonic. This arrangement did not work well because it was very hard to get a suitable pressure of SF_6 at which

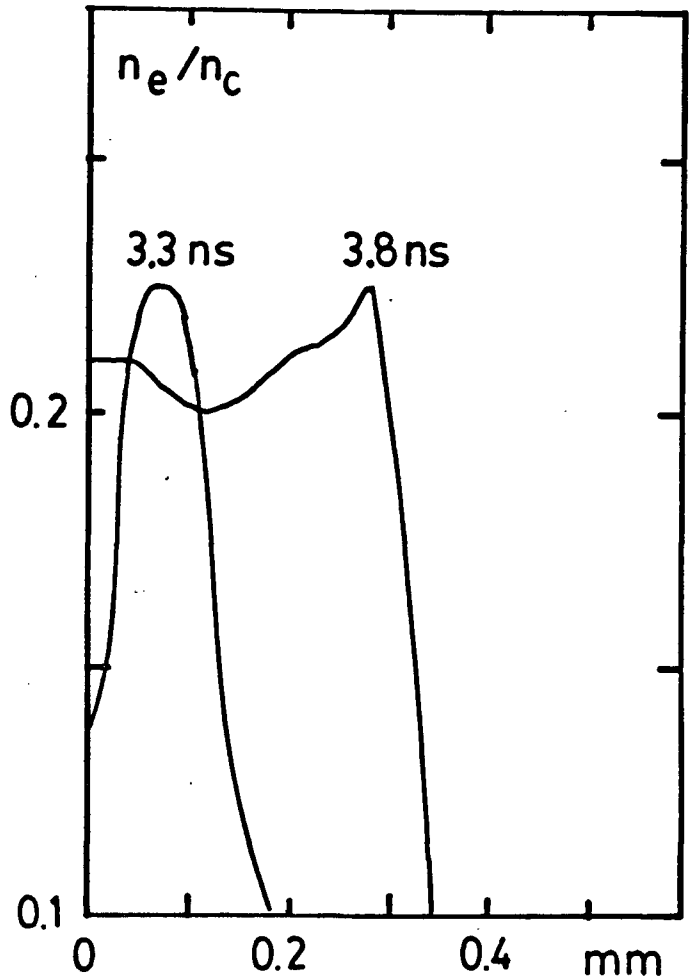

Figure 3-2 Density profiles of the plasma. Radial density profiles of the plasma inside the jet at times t=3.3ns and t=3.85ns after start of the laser pulse

all 10.6μm signal was absorbed while the harmonic signal was transmitted, due to the fact that the scattered signal changed very much from shot to shot. It was also very hard to focus the whole scattered beam on the small sensitive area of the detector with the monochromator. Also with this arrangement, a lot of signal was lost due to the absorption of the SF_6 cell, and reflection losses of the many lenses in the arrangement. Hence the $(3/2)\omega_0$-emission signal obtained by the detector was too small to measure. The arrangement was hard to use to make angular distribution measurements since the arrangement had to be realigned for every angle. An MgF_2 absober was used, instead of the SF_6 cell, to absorb 10.6μm signal. In principle, MgF_2 absorber cannot transmit 10.6μm signal at all, and can transmit

$\sim$ 90% signal in the wavelength range from $1.1\mu m$ to $9.7\mu m$. The measurements proved that MgF_2 absorber works prefectly-the rejection of the $10.6\mu m$ is about 10^{10}. In order to rotate the arrangement around the chamber and to focus the beam on the small sensitive area of the detector easily to make the $(3/2)\omega_0$-emission angular distribution measurements, we used an interference filter, instead of an IR monochromator, to separate the harmonics. When we measured $(3/2)\omega_0$-radiation from backscattering with the arrangement with MgF_2 absorber and a filter(centre wavelength $\lambda_0 = 7.06\mu m$), we got a very small signal $\sim$ 100mV, but without the filter, we got a much bigger signal $\sim$ 3V. Considering that the absorption by the filter of $(3/2)\omega_0$-emission cannot cause the very large difference in the signal, we thought there were other wavelength in the signal besides the $(3/2)\omega_0$-radiation. We used the following methods to identify what the other radiation is.

Firstly, we used the monochromator with the MgF_2 absorber and found there was $5.3\mu m$ radiation in the signal besidesthe $7.06\mu m$($(3/2)\omega_0$-radiation). Secondly, we used $5.3\mu m$ filter with MgF_2 absorber and saw large signal $\sim$ 3V. Thirdly, in order to check in the signal whether there is any other radiation, we used $5.3\mu m$ filter and $10.6\mu m$ filter, and $5.3\mu m$ filter and $7.06\mu m$ respectively with MgF_2 absorber and we did not see any signal. Fourthly, we put plastic glass with $5.3\mu m$ filter and did not see any signal. In the end, with the results of these measurements, we concluded the radiation to be $2\omega_0$-radiation. We can see that the use of the SF_6 cell in the original arrangement is the reason why the second harmonic radiation was not observed before. The final experimental arrangement for the measurement of the angular distribution of the $(3/2)\omega_0$ and $2\omega_0$ harmonics is shown in Fig. 3-3 and includes most of the windows, except the backscattering window. The backscattering was measured with the experimental arrangement as shown in Fig. 3-4.

The cylindrical target chamber contains a series of ports in the horizontal plane, evenly spaced at 18°. Their 5cm diameter subtended an angular range of

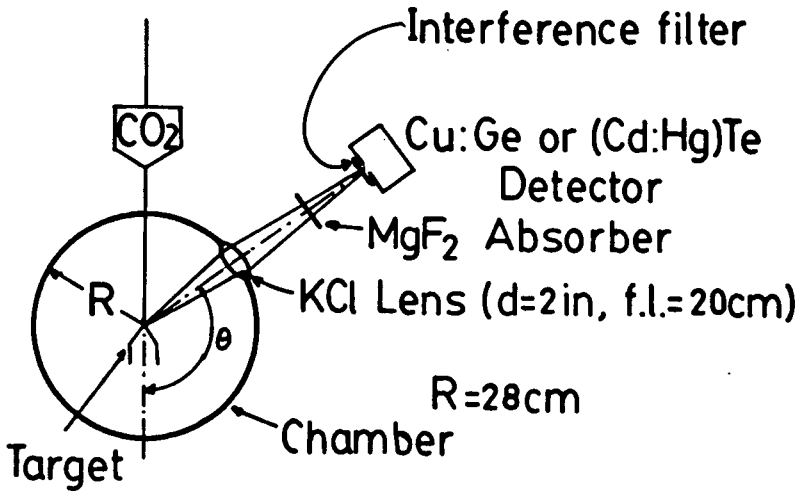

Figure 3-3 Experimental arrangement for angular distribution measurement.

10°to the target. Harmonic-emission outward through individual ports was detected by passing the radiation through a MgF_2 absorber and an interference filter. The filter for $2\omega_0$ is centred at $\lambda = 5.4\mu m$ with a $0.6\mu m$ pass band and a 1 inch diameter. The filter for $(3/2)\omega_0$ is centred at $\lambda = 7.4\mu m$ with a $0.8\mu m$ pass band and a size of $3mm \times 8mm$. The radiation was then focussed onto either a Cu:Ge- or a (HgCd)Te- detector and the signals were displayed by a GHz-oscilloscope(Tektronix 7104 oscilloscope). The combined (HgCd)Te-detector-oscilloscope rise time is 0.5ns and the fall time some what longer.

The experimental arrangement for measurements of the spectra of $(3/2)\omega_0$ and $2\omega_0$ harmonics is shown in Fig.3-5. The combination of the image dissector with an infrared spectrometer permitted the measurement of spectra in the infrared region in a single shot while still using one detecor. The detailed description of the construction of the image dissector can be found in ref. 2 and 39. The image dissector used in this arrangement is almost the same as that J.E. Bernard[2] used before, except that a mirror is used to focus the beam from the monochromator on the entrance window of the image dissector so that we get a same focal point for the signal

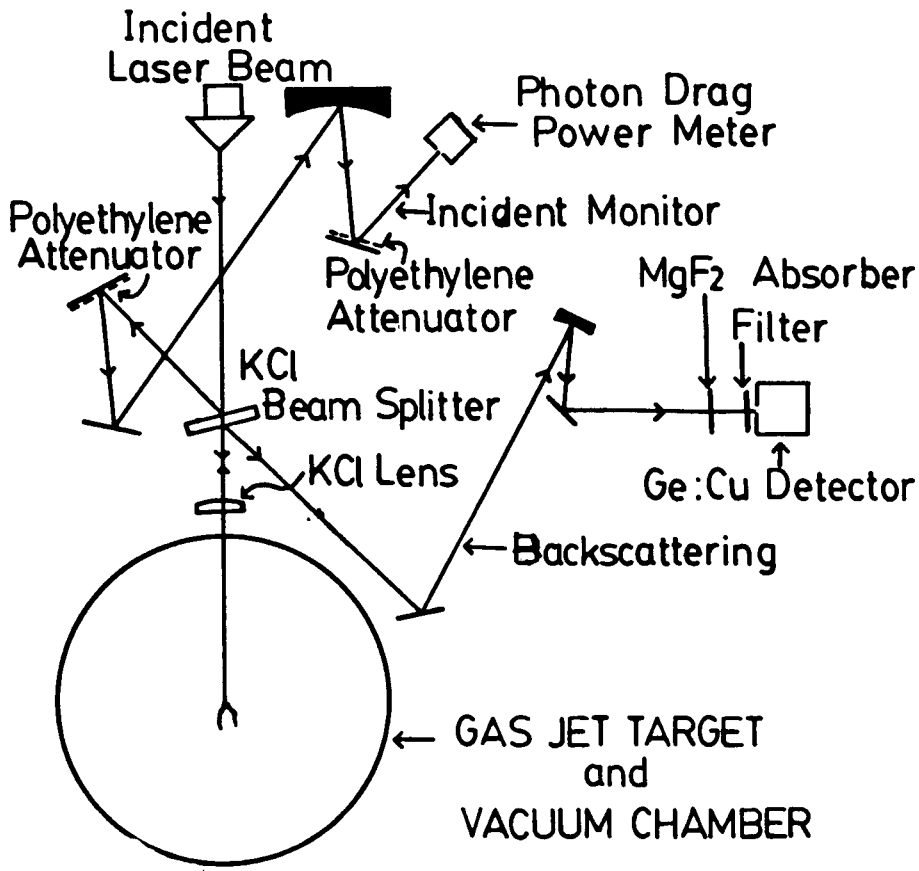

Figure 3-4 Experimental arrangement for the backscattering measurement.

as that for HeNe laser beam when we use a HeNe laser to align the monochromator-image-dissector combination, instead of a KCl lens. A magnified(3.3 times) image of the spectrum at the spectrometer exit-plane is produced at the top edge of the square mirrior, M1, by mirror, M4(4 inch dim., 11 inch f.l.)

The spectrometer image dissector combination was aligned with the aid of a HeNe laser. In order to avoid the differences in the focal position caused by the KCl lens due to the refractive index difference in the chamber for HeNe laser beam and for scattering signals, firstly, we calculate the focal length for scattered beam, f_s and focal length for HeNe laser beam, f_{HeNe} for the KCl lens; secondly, we calculate the image position, i with f_s and object position, o(o=R, R is radius of

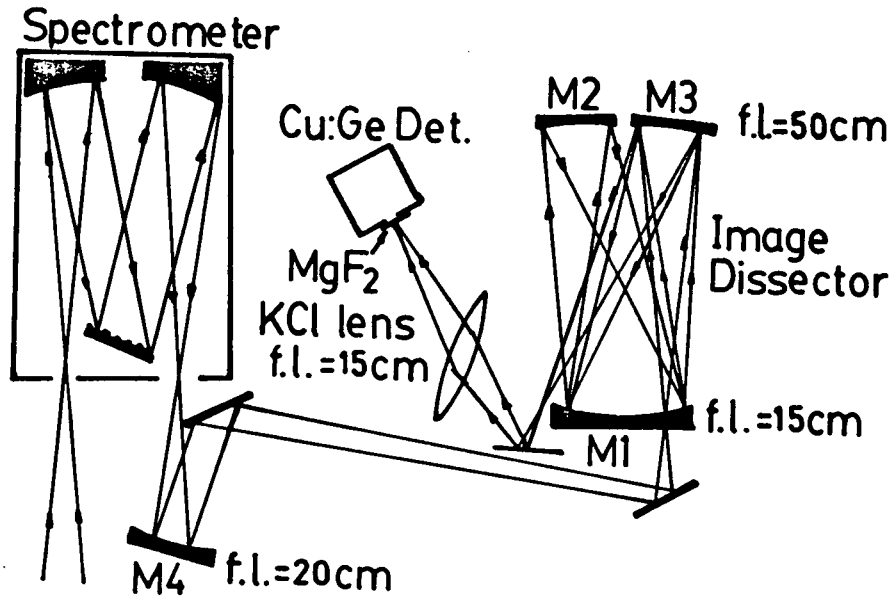

Figure 3-5 Experimental arrangement for spectrum measurement.

the chamber); thirdly, we get another object position o' with i and f_{HeNe}; finally we use a lens(f.l.=10cm) to focus the HeNe laser beam in position o'. In addition, we put some diffuser in position o' so that we get a good focal position. Thus we can use HeNe laser to align the system pretty well as shown in Fig.3-6.

The amplified 2ns pulse emerging from the CO_2 laser K 103 preamplifier as shown in Fig. 3-1, was sent to the spectrometer and was used for calibrating the individual channel response. In order to conveniently obtain the calibration curve, we choose the width of each channel ($\sim 40\mathring{A}$) so that the beam from K 103 is as wide as one channel. A typical calibration curve is shown in Fig.3-7.

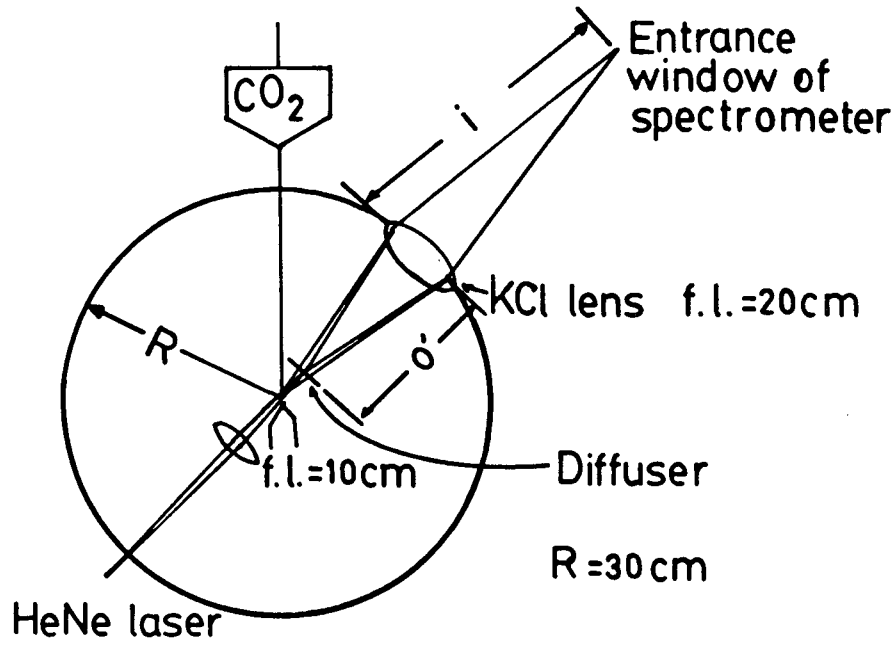

Figure 3-6 Monochromator alignment arrangement.

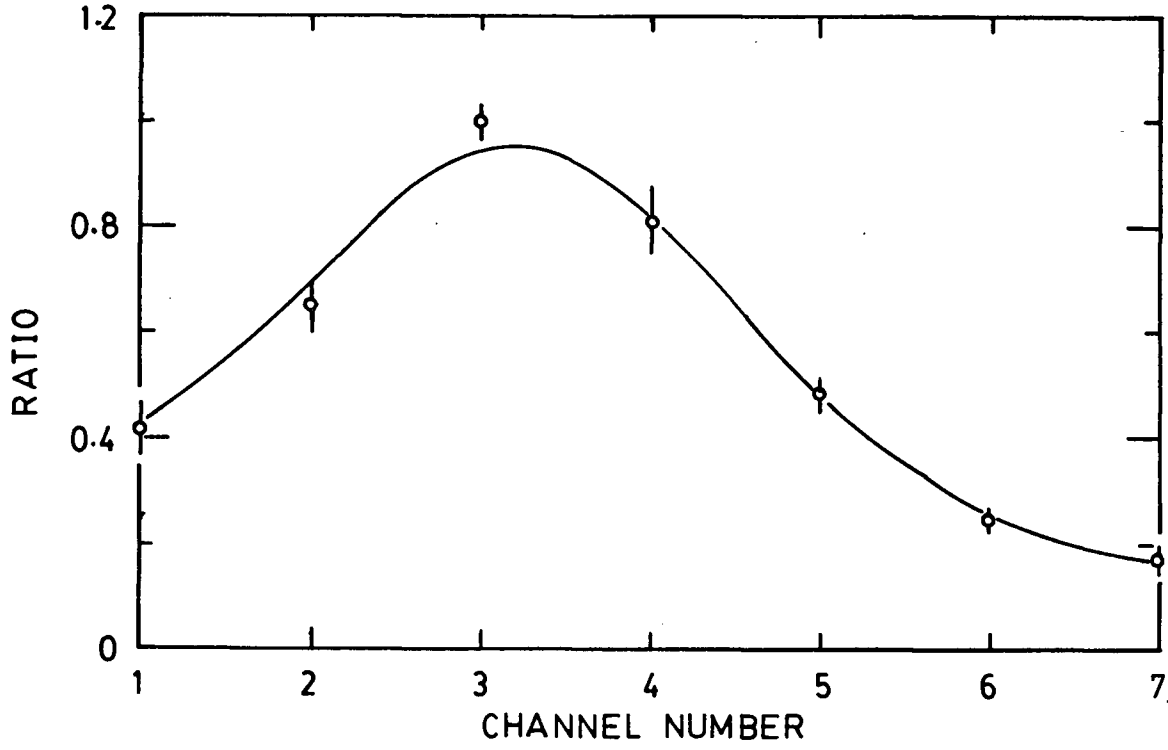

Figure 3-7 Image dissector calibration curve. The error bars are the standard deviation of signals for about 5 shots.

CHAPTER 4

EXPERIMENTAL RESULTS

The results of all measurements of angular distribution, spectra, dependence on target pressure and target material, and on polarization of incident beam, of the $(3/2)\omega_0$ and $2\omega_0$ harmonics are presented in this chapter. The dependence of $(3/2)\omega_0$ and $2\omega_0$ harmonics on incident beam energy is also given. The detailed discussion of the results is left to the next chapter.

4.1 Angular Distribution

Most of the $(3/2)\omega_0$ and $2\omega_0$ measurements, except the measurements of dependence of the $(3/2)\omega_0$ and $2\omega_0$ on the incident beam polarization, were performed in the plane of polarization (i.e. the plane of $\mathbf{E}_0$ and $\mathbf{k}_0$, in later time we call this plane as horizontal plane, the plane perpendicular to this plane we call vertical plane) of the incident laser radiation. In most directions, except in forward direction $\theta = 0°$, the Ge:Cu detector was used. At $\theta = 0°$, in order to prevent the expensive Ge:Cu detector from being damaged by the strong incident laser beam, a (HgCd)Te detector(generally called, the 'Polish detector') was used. The (HgCd)Te detector was calibrated in the other windows against the Ge:Cu detector, and the equivalent signal for the Ge:Cu detector in the forward direction was obtained. The backscattering was measured with the experimental arrangement as shown in Fig.3-4 different from that as shown in Fig.3-3 used in sidescattering measurements. In calibrating the backscattered signal, we took into account the reflection of the salt

flat (the beam splitter), and the area difference of the windows, and assumed that backscattering beam passes evenly through the whole incident beam focal lens. For most measurements, except the measurement of the target pressure dependence, the nitrogen target reservoir pressure TP_0 was 31.5PSI, and the background helium pressure was 5 Torr.

As the **k**-vector matching conditions govern the generation of the harmonics in the laser–plasma interaction, we think the angular distribution is a signature of the harmonics. In order to confirm the predicted mechanism for the harmonics, first we made the angular distribution measurement of the $(3/2)\omega_0$ and $2\omega_0$ harmonics. We made about 50 shots in each window for $(3/2)\omega_0$ and $2\omega_0$ harmonics respectively. The incident laser beam energy varies from about 1J to about 10J. We grouped these shots in the energy bins which are 1J wide(i.e. 0.1–1J shots were grouped, 1.1–2J shots were grouped, etc.). Fig. 4–1 shows the angular(θ) distribution of $2\omega_0$ power for four different energy bins emitted into $d\Omega = \pi r^2/R^2$(where r is the radius of the window, R is the radius of the chamber). The error bars represent the standard deviation of the mean of the signal from about 5 shots. The $P_{2\omega_0}$ in Fig. 4–1 is the orignal signal we measured and is:

$$\begin{aligned} P_{2\omega_0}(\theta, \Phi = 0) &= I_{2\omega_0} \cdot \pi r^2 \\ &= I_{2\omega_0} \cdot R^2 d\Omega. \end{aligned}$$

Since $d\Omega = \sin\theta d\Phi d\theta = (\pi r^2)/R^2$ =constant and $d\theta = 10^\circ$ for every window, $d\Phi$ is a function of $\sin\theta$. In order to check our theoretical prediction about the angular distribution of $2\omega_0$ from eq. (2–33) as $\triangle\Phi = 1rad$ in Chapter 2, we modify the original signal $P_{2\omega_0}$ by a factor α:

$$P'_{2\omega_0} = \alpha P_{2\omega_0}(\theta, \Phi = 0).$$

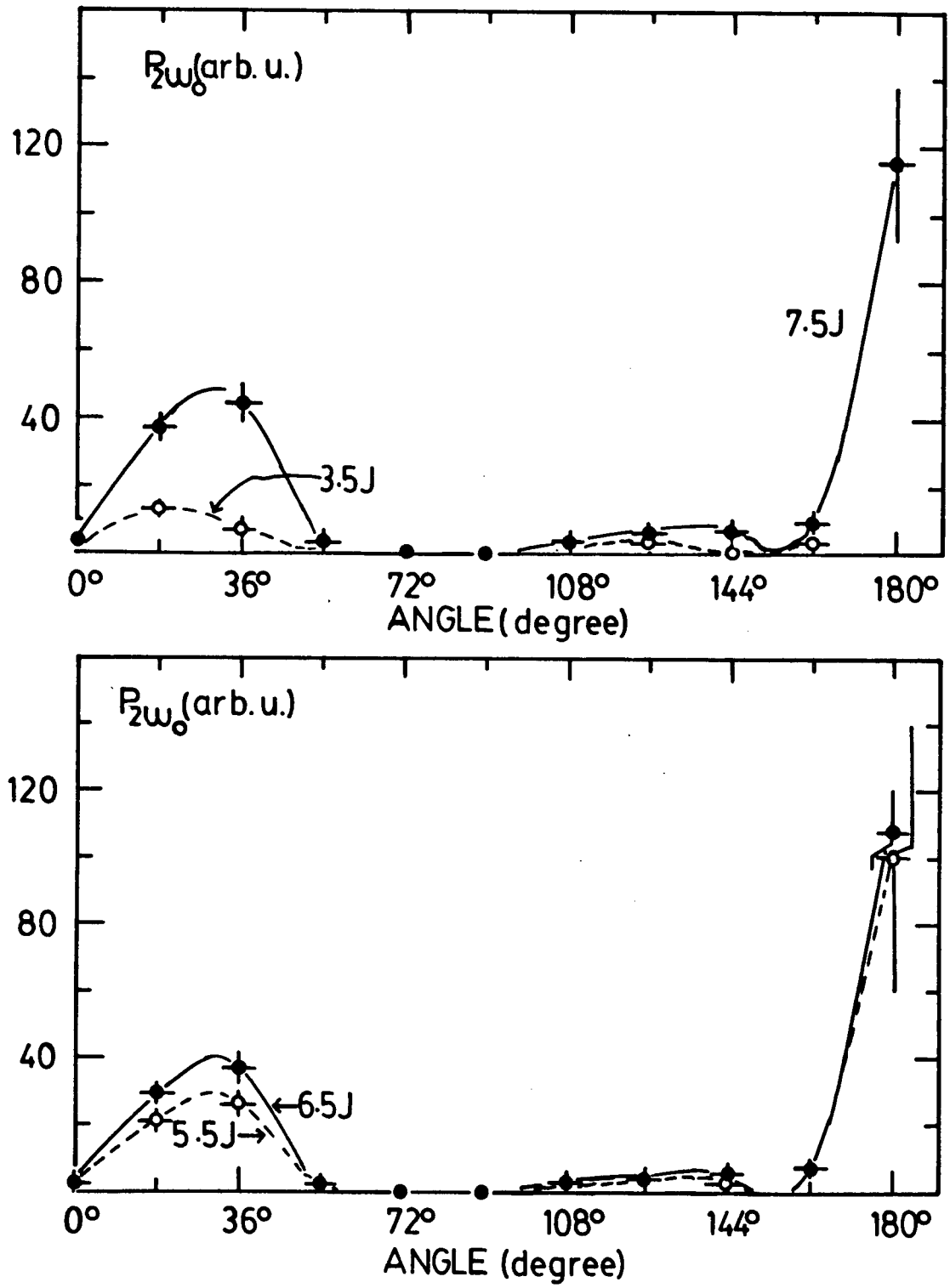

Figure 4-1 Angular distribution of $2\omega_0$ for solid angle $d\Omega$ =constant.

Here

$$\alpha^{-1} = \begin{cases} 2\pi & \theta = 0°,\ 180°; \\ \frac{2\pi 2\pi R \sin\theta \cdot 2r}{\pi r^2} & \text{in other direction.} \end{cases}$$

The angular distribution of $P'_{2\omega_0}(\theta) - \theta$ is shown in Fig. 4-2. The emission strongly peaks in the forward direction around $\theta = 30°$. However, a broad angular distribution of $2\omega_0$-radiation emitted in the backward direction peaked near $\theta = 130°$ is as well present. The shapes of the angular distribution of $2\omega_0$ emission are almost the same for four different energy bins, as only the heights of peaks increase with the increases of the incident beam energy. Thus one can conclude that the the angular distribution of $2\omega_0$-emission is independent on the incident beam energy.

The forward peak at $\theta = 36°$ in the angular distribution of $2\omega_0$ radiation confirms the prediction given in Chapter 2. Thus we can think this is due to the filamentation. The non-negligable backward emitted $2\omega_0$ radation over a broad angular range near $\theta = 130°$ is not expected, perhaps it is due to the coupling of the incident beam with the backscattered wave produced in the SBS instability.

The absolute scale for $P_{2\omega_0}$ in Fig.4-2 is based on an estimate which takes the detectivity of the detectors into account. Due to the small detector area($1mm^2$) this estimate is only a lower limit accurate to within a factor of two.

Fig. 4-3 shows the angular(θ) distribution of $(3/2)\omega_0$ power for five different energy bins emitted into $d\Omega = (\pi r^2)/R^2$. The shapes of the angular distribution of $(3/2)\omega_0$ emission are different for different energy bins. For high energy bins ($W_L = 8.5J, 7.5J$), we can see three peaks(perhaps four peaks, peaks at $\theta = 36°, \theta = 108°$, and $\theta = 144°$ are very obvious, but peak at $\theta = 72°$ is not clear); for low energy bins($W_L = 4.5J$ and $5.5J$), $(3/2)\omega_0$-radiation emitted over a broad angular range around $\theta = 126°$, and weakly emitted in the forward direction at $\theta = 36°$ and $\theta = 72°$. The peaks in the backward direction are stronger than that in the forward direction for all energy bins.

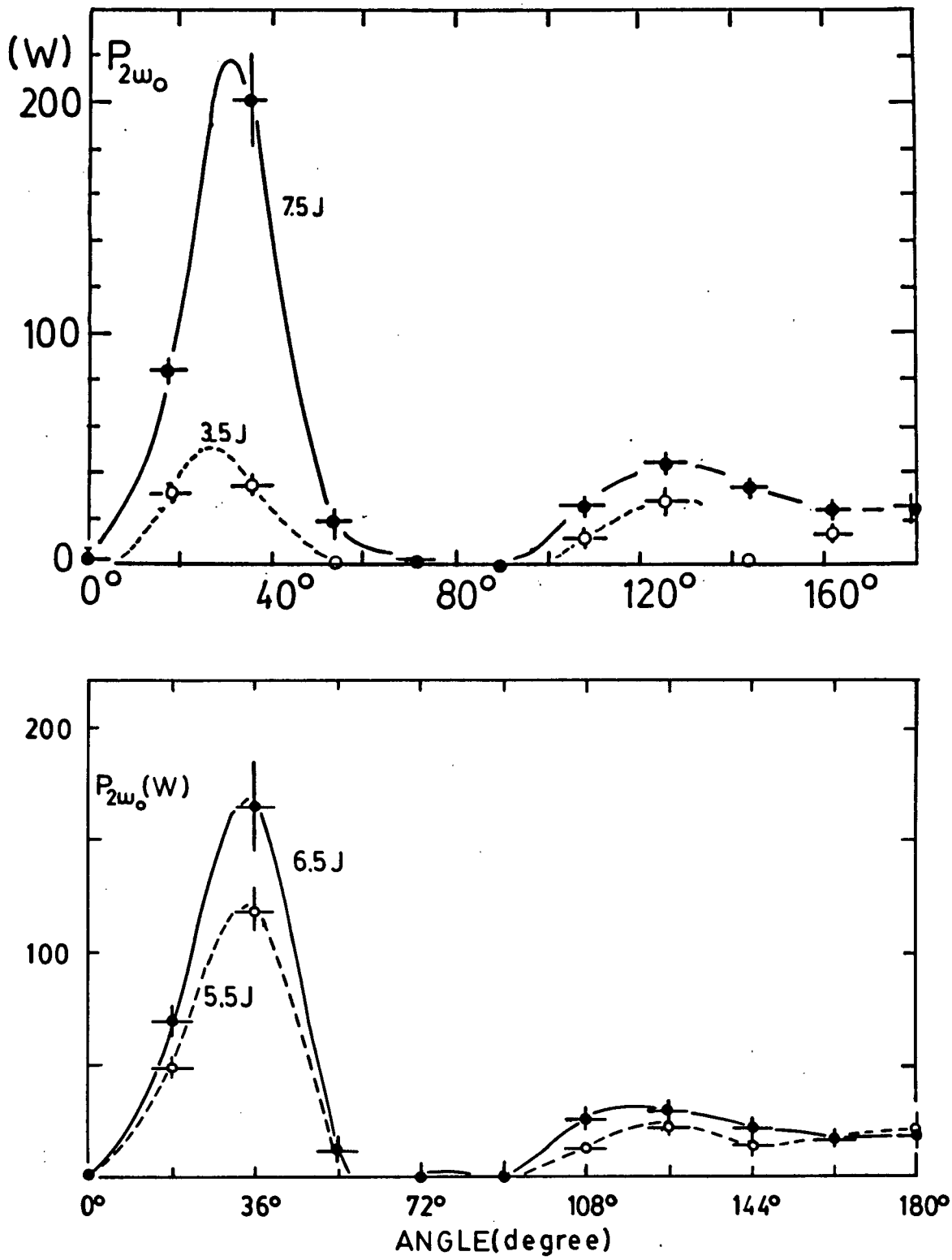

Figure 4-2 Angular distribution of $2\omega_0$ for $\triangle\Phi = 1 rad.$

In Chapter 2, based on the wave vector matching conditon, we predicted that $(3/2)\omega_0$-radiation should peak at $\theta = 71°$ and $\theta = 109°$(due to the first mechanism: the coupling of the incident beam with the plasma wave produced in the TPD instability), and at $\theta = 38°$ and $\theta = 142°$(due to the second mechanism: the fusion fo three plasma waves produced in the TPD instability); the peaks in the backward direction are stronger than those in the forward direction for both mechanisms. Our observation obviously confirms the peaks at $\theta = 38°$ and $\theta = 142°$, but does not obviously confirm the peaks at $\theta = 71°$ and $\theta = 109°$. For high energy bins, the peak at $\theta = 108°$ is clear, while the peak at $\theta = 72°$ is not obvious as we consider the error bars; for low energy bins, $(3/2)\omega_0$-radiation at $\theta = 108°$ is as strong as at $\theta = 144°$. If we assume our prediction is right, then we see at low incident beam energy, the first mechanism and the second mechanism almost equally contribute to the generation of $(3/2)\omega_0$-radiation, at high incident beam energy, the second mechanism dominates the generation of $(3/2)\omega_0$-radiation. We know the second mechanism is one order higher nonlinear process than the first mechanism. How the higher order nonlinear process is stronger than the lower order one is hard to understand. We will try to answer this question in next chapter.

The dependence of $2\omega_0$-emission on incident laser power is indicated in Fig. 4-4 where $P_{2\omega_0}$ is plotted as function of the square of the incident laser energy W_L. Fig. 4-4 (a) and (c) show that the emitted $2\omega_0$ power at $\theta = 18°$ and $\theta = 144°$ increase proportionally to W_L^2 once the laser energy surpasses 3J. For $2\omega_0$ radiation emitted in other directions, however, this simple power law dependence is not nicely satisfied as shown in Fig. 4-4 (b), (c) and (d) where $P_{2\omega_0}$ for $W_L > 3J$ increases at a rate nonlinear in W_L^2. The square law dependence of $2\omega_0$ power at $\theta = 18°$ is as well demonstrated in Fig. 4-5 showing (a) $P_{2\omega_0}(t)$ and (b) $P_{2\omega_0}^{1/2}(t)$ compared to P_{ω_0}. The observation confirms the theoretical prediction from eq. (2-33) that the $2\omega_0$ radiation generated by the filamentation is proportional to the square of the incident beam power.

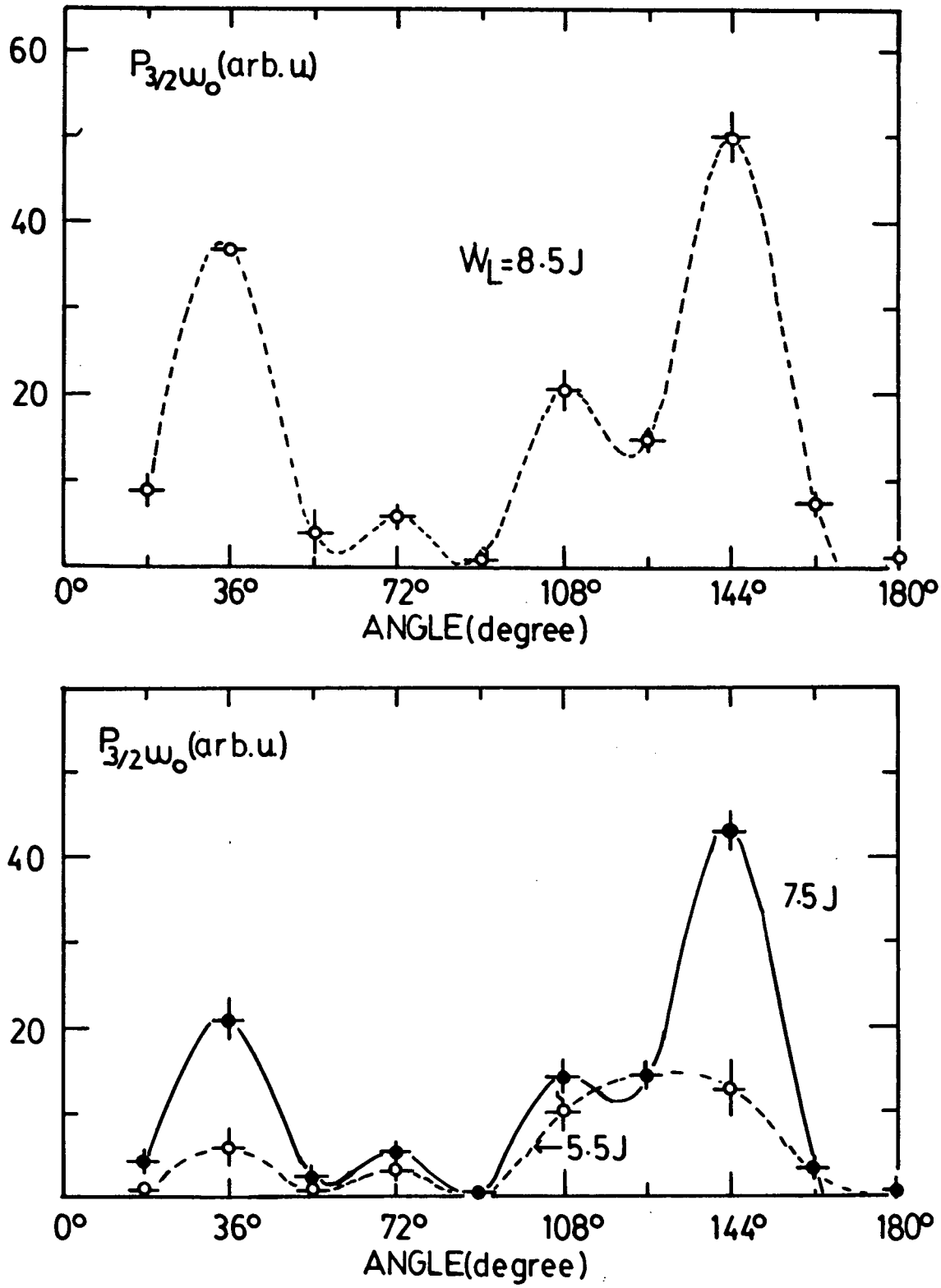

Figure 4-3 Angular distribution of $(3/2)\omega_0$ as $d\Omega$ =constant.

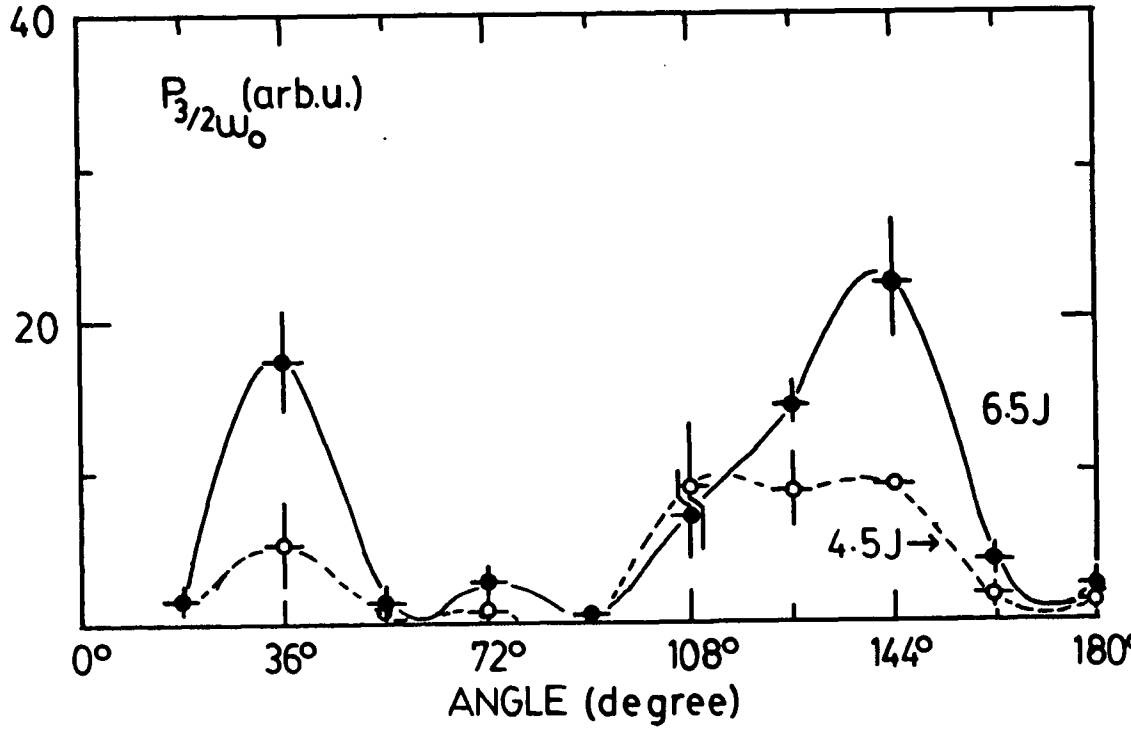

Figure 4-3 Continued.

The dependence of $(3/2)\omega_0$-emission on incident laser energy is shown in Fig. 4-6 where the reflectivity is defined as the ratio of the amount of $(3/2)\omega_0$ emission to the incident radiation. From Fig. 4-6(a),(b),(c) and (d), one can see that in different directions, the reflectivity curves are not the same. In $\theta = 18°, 36°, 54°, 144°$ and $162°$, $(3/2)\omega_0$-emission does not saturate as laser energy $W_L = 9.5J$, but in $\theta = 72°, 108°$, and $126°$, $(3/2)\omega_0$-emission saturates by $W_L = 8.5J$. Hence, the relation between $(3/2)\omega_0$-emission and incident beam energy is not simple and depends on the directions.

The result of the angular distribution measurement of the harmonics gives us much evidence about the mechanism of the generation of the harmonics. In next

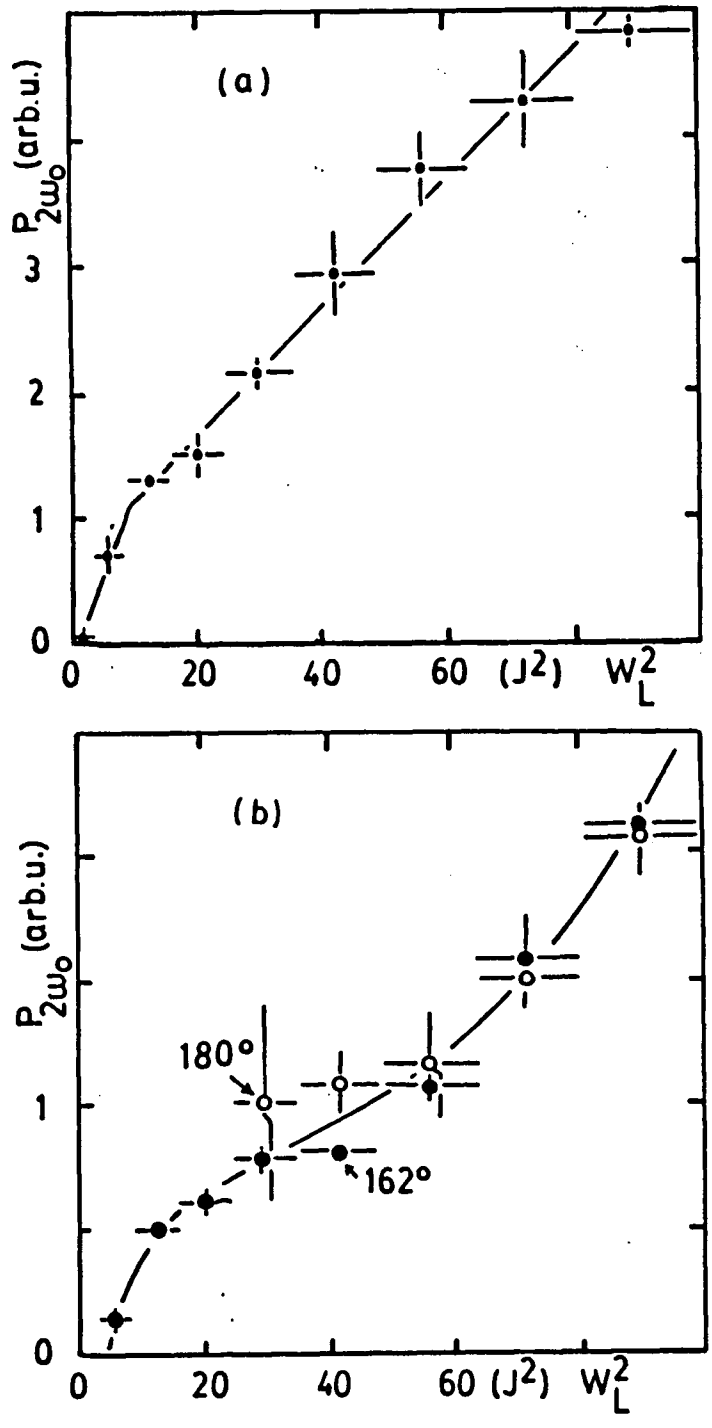

Figure 4-4 $2\omega_0$ power as function of the square of the incident laser energy. The error bars for $P_{2\omega_0}$ indicate the standard deviations of several signals and for W^2 the width of the energy bins. Fig. (a) shows the signals at $\theta = 18°$, (b) those at $\theta = 162°$ and $\theta = 180°$, (c) those at $\theta = 36°$ and $\theta = 144°$, (d) those at $\theta = 126°$ and $\theta = 54°$.

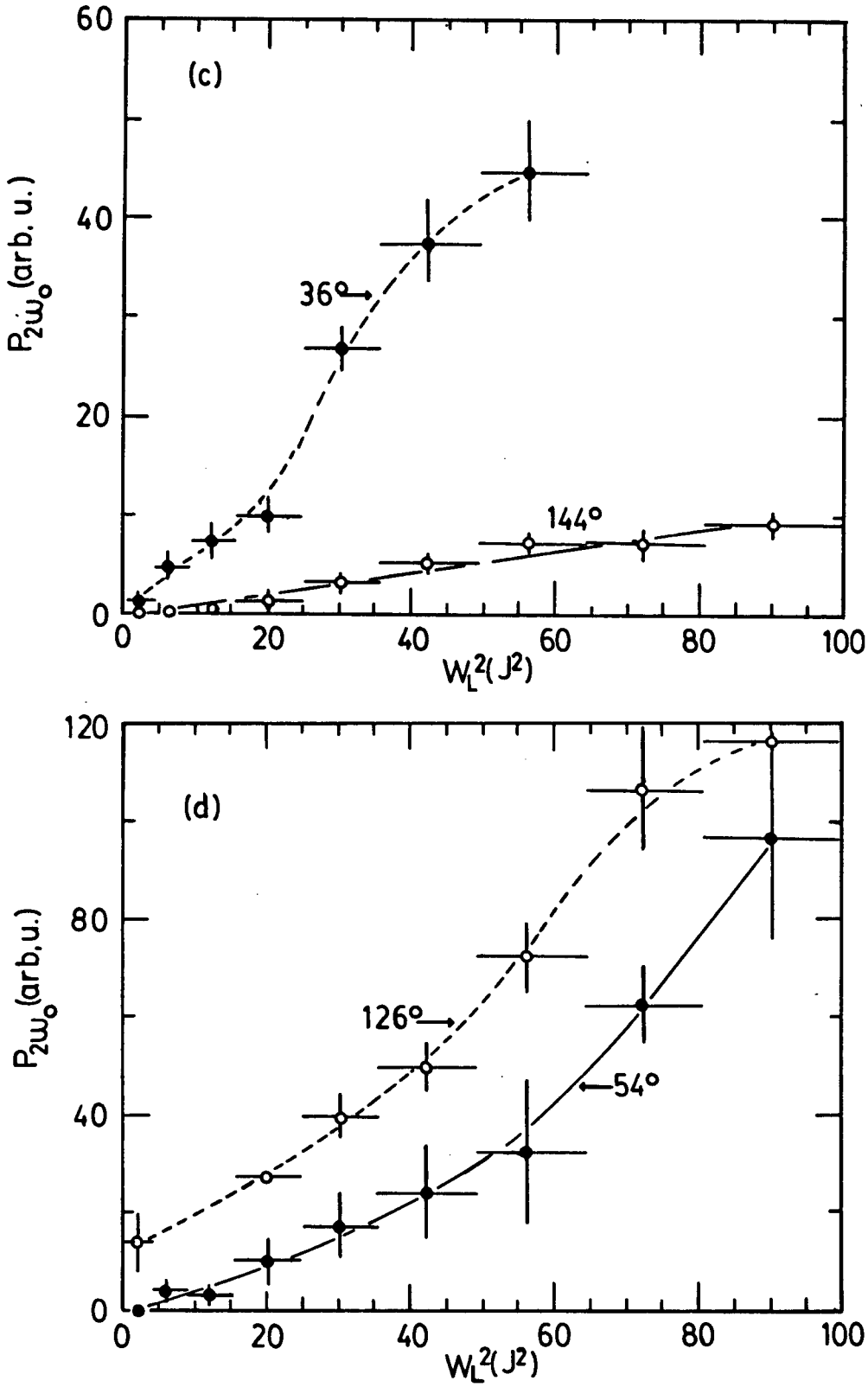

Figure 4-4 Continued.

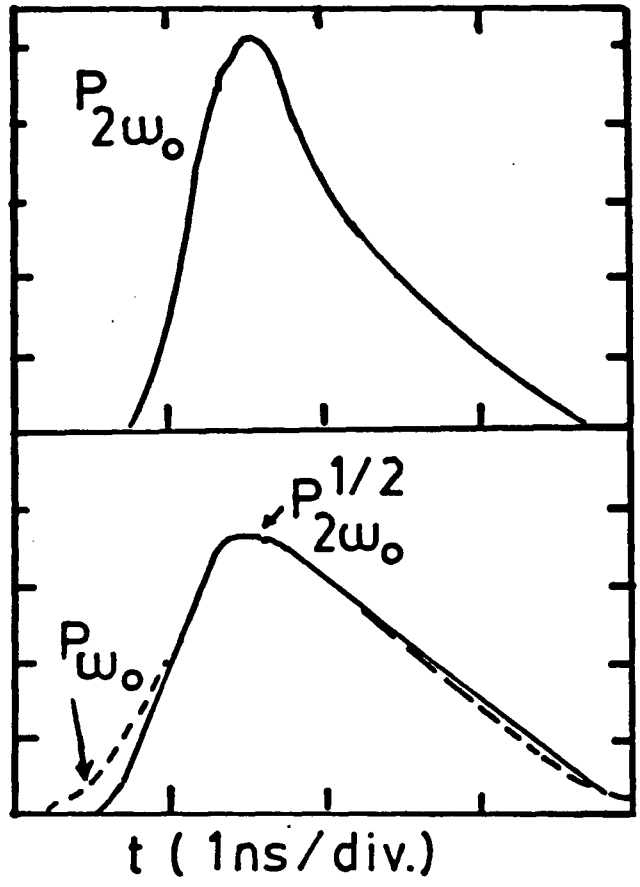

Figure 4-5 Time evolution of $P_{2\omega_0}$. Fig.(a) $P_{2\omega_0}(t)$ at $\theta = 18°$ Fig.(b) The laser pulse compared to $[P_{2\omega_0}(t)]^{1/2}$

section we examine the frequency spectra of the harmonics and try to obtain more information for the mechanism of the generation of the harmonics.

4.2 Spectra

Some scope traces of output from the Image Dissector are shown in Fig. 4-7. Fig. 4-7 (a) and (b) are for $(3/2)\omega_0$ radiation at $\theta = 144°$, (c) for $2\omega_0$ radiation at $\theta = 18°$, and (d) for $2\omega_0$ radiation at $\theta = 162°$. The spectra for forward($\theta = 18°$) and backward($\theta = 162°$) emitted $2\omega_0$ radiation in Fig.4-8 show some significant differences. At $\theta = 18°$ the spectrum is centred at $\lambda_0/2$ having a width of $(80 \pm 5)\mathring{A}$. Subtracting the instrument width of $40\mathring{A}$ leads to an estimate of a FWHM spectral

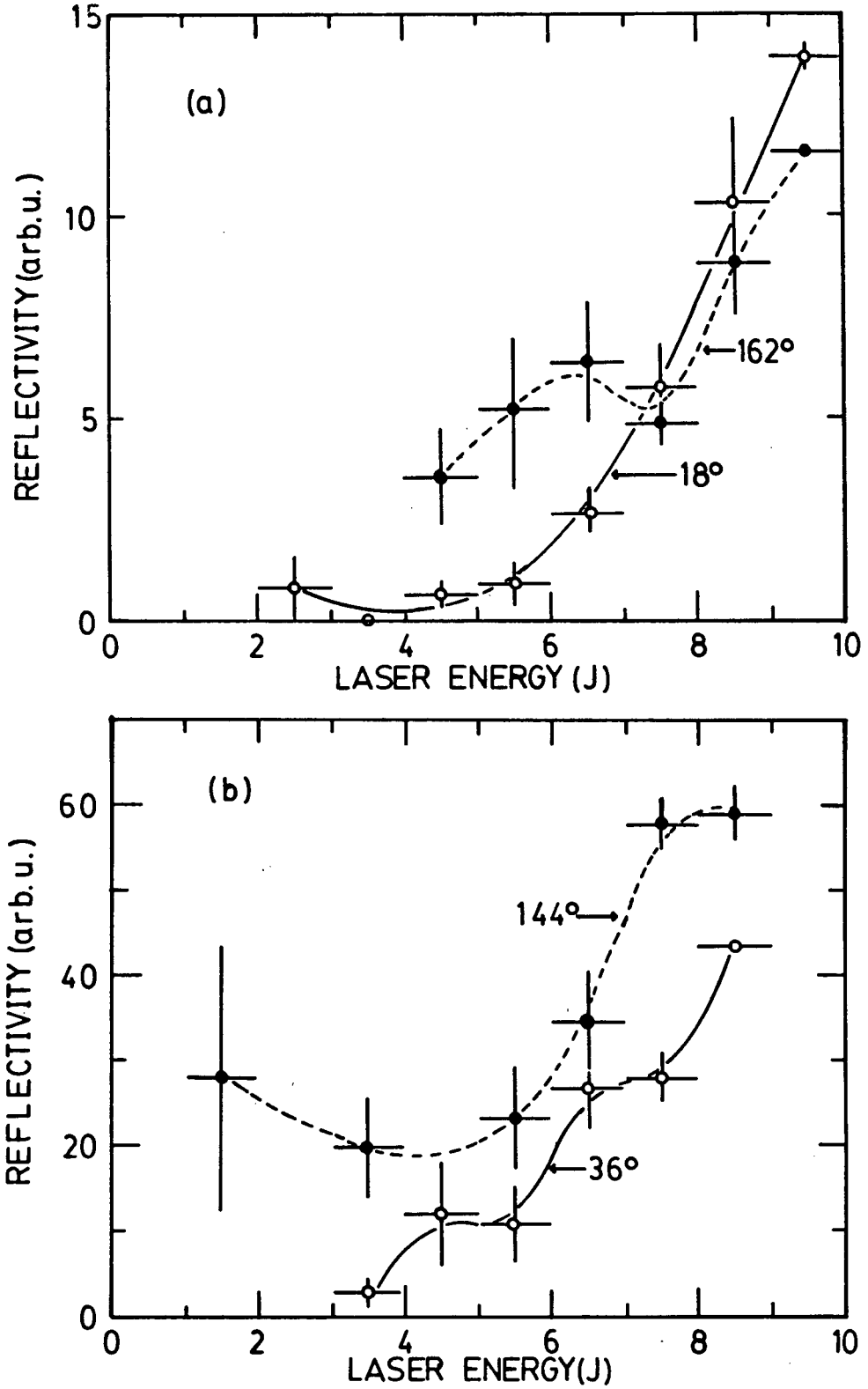

Figure 4-6 Reflectivity of $(3/2)\omega_0$-emission.

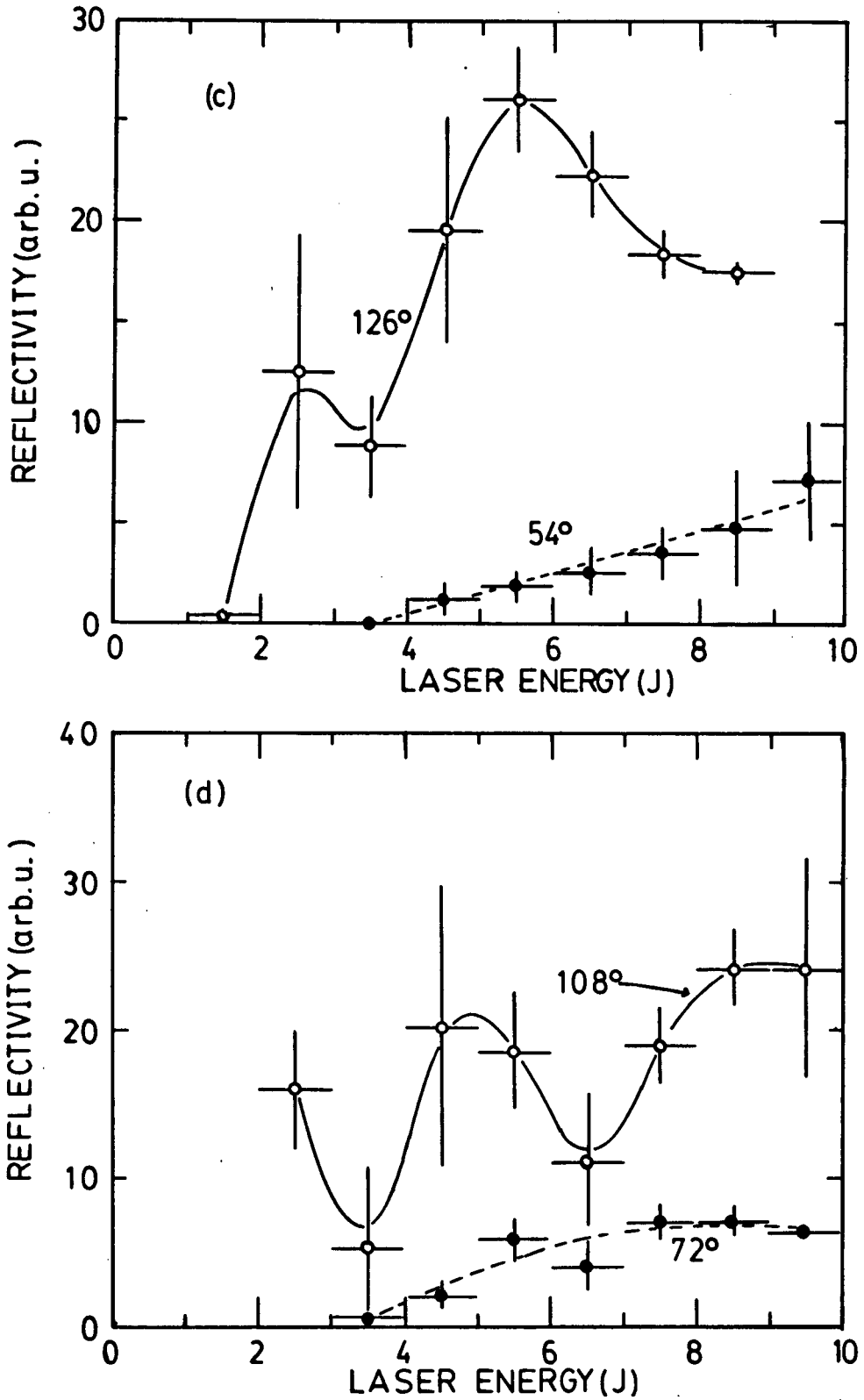

Figure 4-6 Continued.

width of $\sim 70\mathring{A}$. At $\theta = 162°$ the FWHM spectral width, estimated in the same way, is about twice as large. In addition the centre line is always red shifted by $40 \sim 60\mathring{A}$.

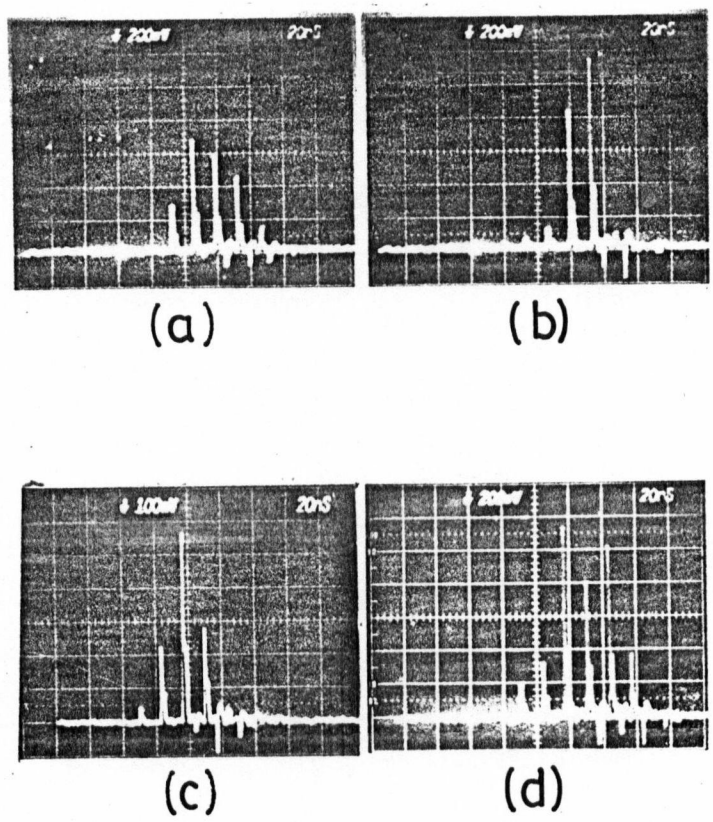

Figure 4-7 Scope traces of output from the Image Dissector. (a) and (b) are for $(3/2)\omega_0$ radiation at $\theta = 144°$, (c) for $2\omega_0$ radiation at $\theta = 18°$, and for $2\omega_0$ radiation at $\theta = 162°$.

Fig.4-9 shows the spectra for backward ($\theta = 144°$) emitted $(3/2)\omega_0$ radiation. It is obviously seen from Fig.4-9(a) and (b) that the amount of the wavelength shift of $(3/2)\omega_0$ radiation and the spectral width depend on the incident beam energy. For lower energy ($W_L = 6.2J$) the spectrum is of the FWHM spectral width of $155\mathring{A}$ with $120\mathring{A}$ red shift. For a little high energy ($W_L = 7.8J$) the spectrum

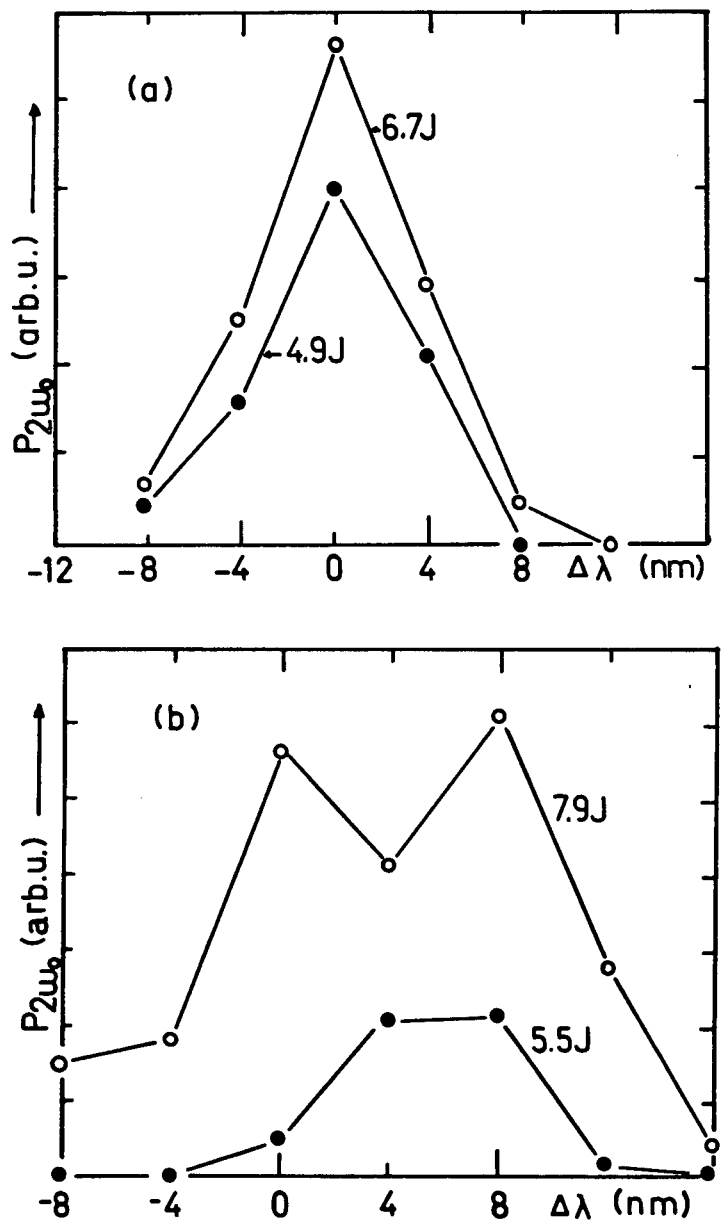

Figure 4-8 $2\omega_0$ spectrum. Second harmonic spectrum for two laser energies (a) at $\theta = 18°$ and (b) at $\theta = 162°$

is centred at $2/3\lambda_0$ having a FWHM spectral width of $\sim$ 101Å(so large variation of the spectrum is perhaps due to the low repeatability of the system with the Spectrometer-Image-Dissector combination). There is only one satellite (red shift) in the spectra.

The spectrum for forward ($\theta = 36°$) emitted $(3/2)\omega_0$ radiation cannot be obtained. This is perhaps because the $(3/2)\omega_0$ radiation has a too wide spectrum in the forward direction to be measured with Spectrometer–Image Dissector combination.

4.3 Time Evolution of the Harmonics

From ref. 2 and 7, we know that the SBS instability and the TPD instabilty have temporal behaviour. We think the backward emitted $2\omega_0$ radiation is related to the SBS instability, and $(3/2)\omega_0$ radiation is related to the TPD instability, therefore it is important for us to examine the time evolution of the harmonics. The scope traces of $2\omega_0$ radiation at $\theta = 18°$ are shown in Fig. 4-10. It looks like from this trace that $2\omega_0$ radiation has two temporal processes. In order to check whether the temporal processes in the trace are due to the detector or are real temporal behaviour, we measured the same signal with different detecors and different signals with the same detector. Fig.4–10 (a) is the trace of $2\omega_0$ radiation at $\theta = 18°$ detected with Ge:Cu detector, (b) with (HgCd)Te detector; (c) is the trace of $(3/2)\omega_0$ radiation at $\theta = 18°$ detected with Ge:Cu detector; (d) is the trace of $2\omega_0$ at $\theta = 162°$ detected with (HgCd)Te detector; (e) is the trace of the CO_2 laser pulse detected with (HgCd)Te detector; and (f) is the trace of a very short pulse with 530ps FWHM detected with (HgCd)Te detector. Comparing all these traces, we can conclude that $2\omega_0$- and $(3/2)\omega_0$- radiation indeed show two time processes.

Some scope traces of $2\omega_0$ harmonic in most windows, except $\theta = 72°$, and $\theta = 0°$, are shown in Fig. 4-11. Fig. 4-11(a) is taken at $\theta = 18°$, (b) at $\theta = 36°$, (c) at $\theta = 54°$, (d) at $\theta = 90°$, (e) at $\theta = 108°$, (f) at $\theta = 126°$, (g) at $\theta = 144°$, (h) at $\theta = 162°$, and (i) at $\theta = 180°$. For each window, the shape of the signals is

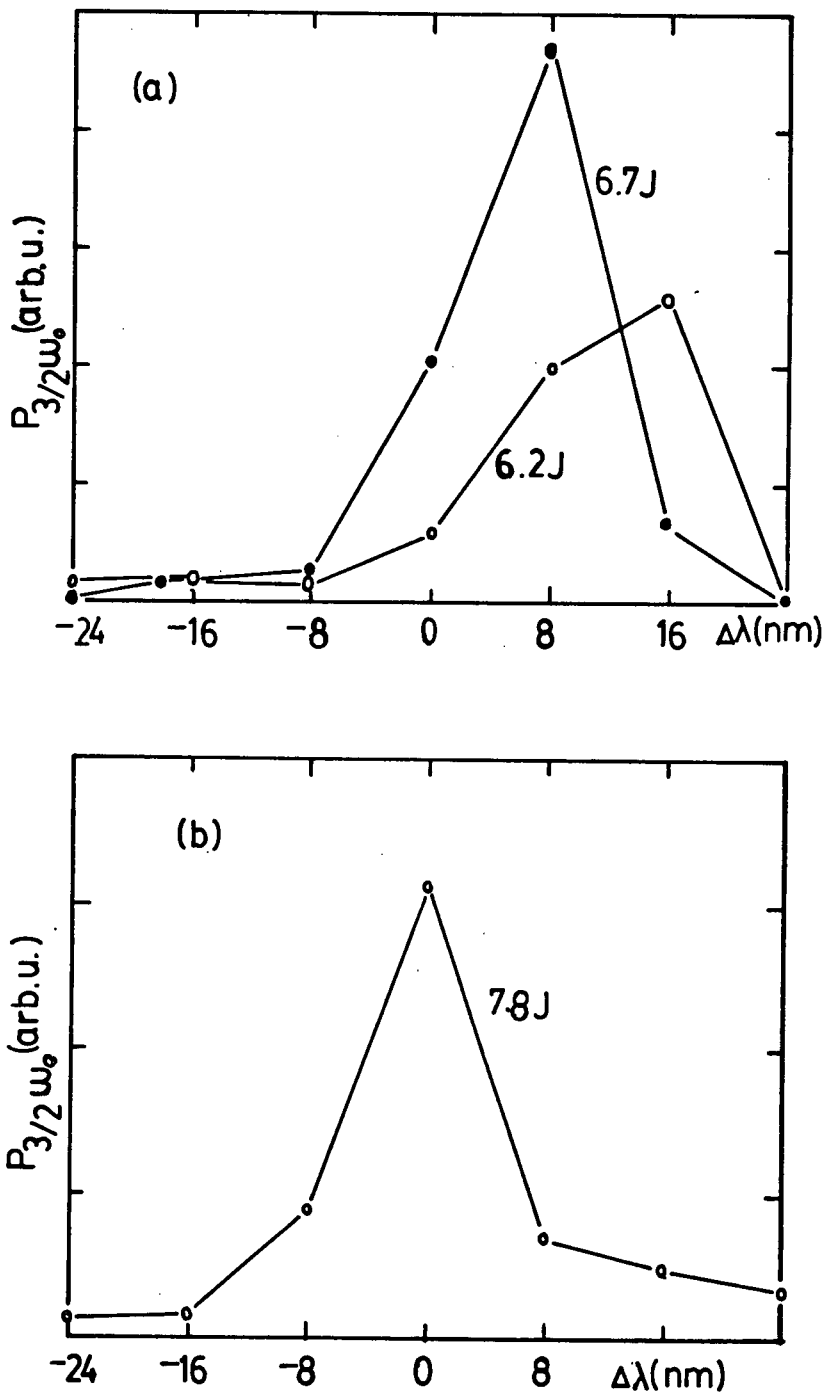

Figure 4-9 $(3/2)\omega_0$ spectrum. $(3/2)\omega_0$ spectrum for three laser energies at $\theta = 144°$

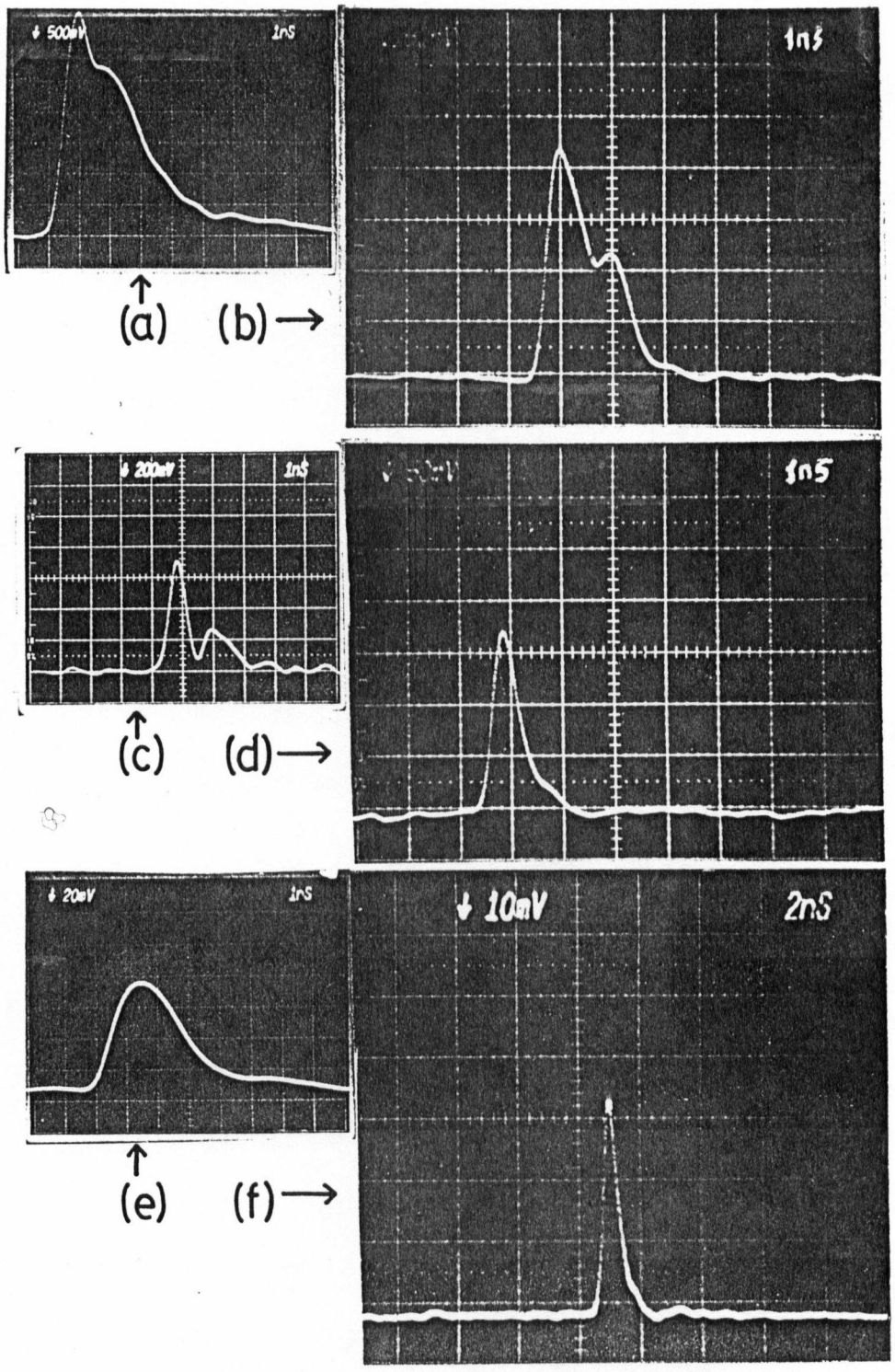

Figure 4-10 Comparation of scope traces. (a)trace of $2\omega_0$ at $\theta = 18°$ detected with Ge:Cu detector, (b) with (HgCd)Te detector; (c) $(3/2)\omega_0$ at $\theta = 18°$ with Ge:Cu; (d) $2\omega_0$ at $\theta = 162°$ with (HgCd)Te; (e) CO_2 laser pulse with (HgCd)Te; and (f) a very short pulse with 530ps FWHM with (HgCd)Te.

always the same. Comparing the traces from different windows, we can infer that the temporal behaviour of $2\omega_0$-radiation is not the same in different directions.

Comparing the scope traces of $(3/2)\omega_0$-radiation for most windows as shown in Fig. 4-12(a–i,$\theta(18° - 162°)$), we can see that the temporal behaviour of $(3/2)\omega_0$-radiation in most directions, except $\theta = 90°$, is almost the same. Since the rise time of the scope and the detector is about 500ps, we cannot know exactly from the scope traces how long each temporal process lasts as the pulse is about 1ns. We estimate the duration of each temporal process to be less than 300ps.

4.4 Pressure Dependence

As mentioned in Chapter 2, each nonlinear process can only occur in some plasma density region. Hence the mesurement of the dependence of the harmonics on the plasma density can give us some important information for understanding the generation of the harmonics. In order to understand the relation between $(3/2)\omega_0$, $2\omega_0$ -emission and the plasma density, we measure $(3/2)\omega_0$ and $2\omega_0$ radiation in both nitrogen and helium gas jet targets at some directions in different pressures since the plasma density depends on the target pressure. The dependence of forward ($\theta = 18°$) emitted $2\omega_0$ radiation on the target pressure in Fig. 4-13 (a) ($W_L = 6.5J$) and Fig. 4-13 (b) ($W_L = 4.5J$) where TP_o is normal target pressure in which the target pressure is 31 PSI, the background helium pressure is 5 Torr, and TP changes with constant N:He ratio, shows that at lower pressure ($TP/TP_0 \leq 2$) $2\omega_0$ power is stronger in the nitrogen target than in the helium target; and at high pressure ($TP/TP_0 > 2$) $2\omega_0$ power increases with the helium target pressure and decreases with the nitrogen target pressure, and gets stronger in the helium target than in the nitrogen target. Fig. 4-13 (c) shows that in the backward direction ($\theta = 162°$) $P_{2\omega_0}$ has the same dependence on the both target pressures, only $P_{2\omega_0}$ is a little larger in the nitrogen target than in the helium target.

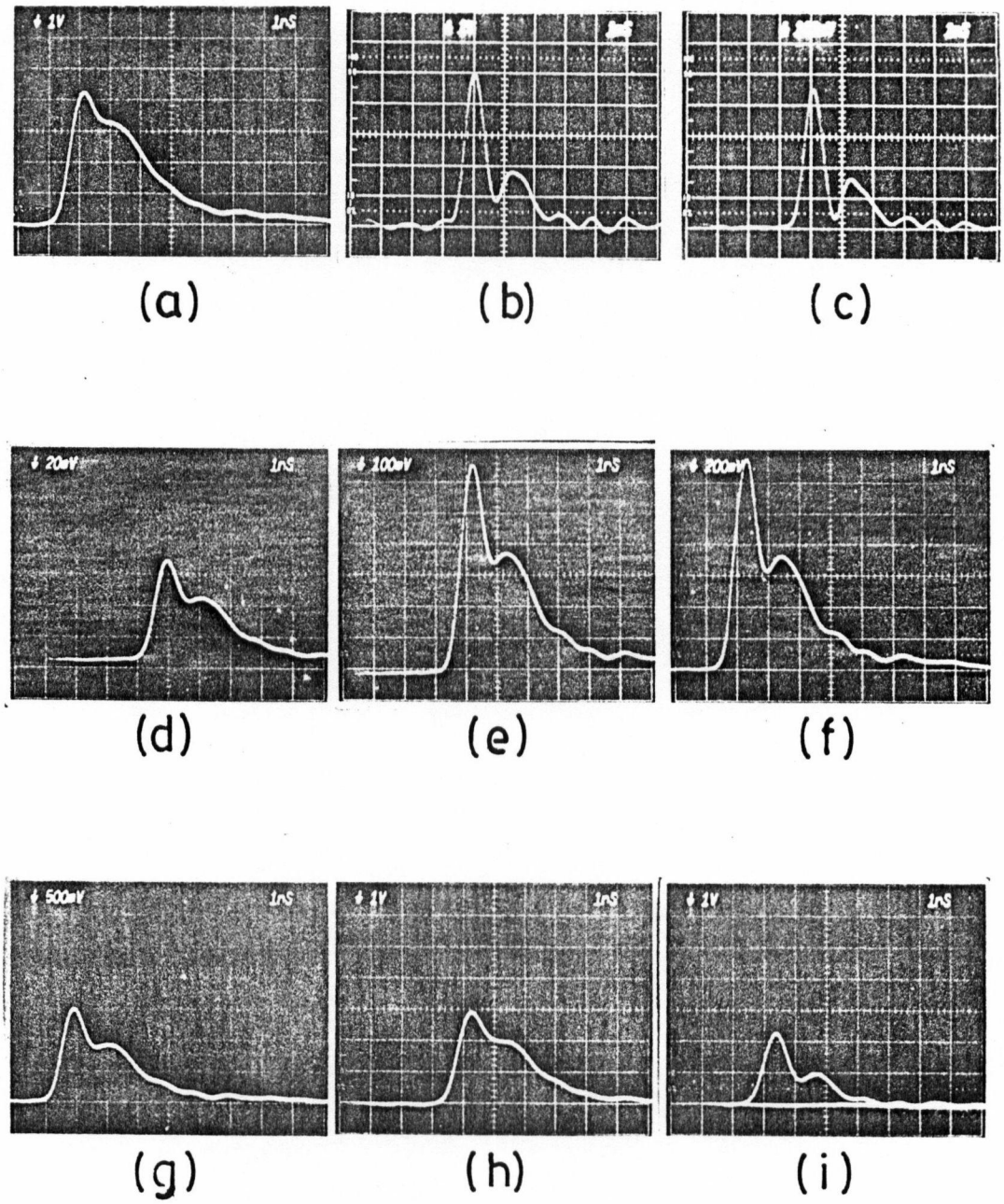

Figure 4-11 Scope traces of $2\omega_0$. In (a) $\theta = 18°$, (b) $\theta = 36°$, (c) $\theta = 54°$, (d) $\theta = 90°$, (e) $\theta = 108°$, (f) $\theta = 126°$, (g) $\theta = 144°$, (h) $\theta = 162°$, (i) $\theta = 180°$.

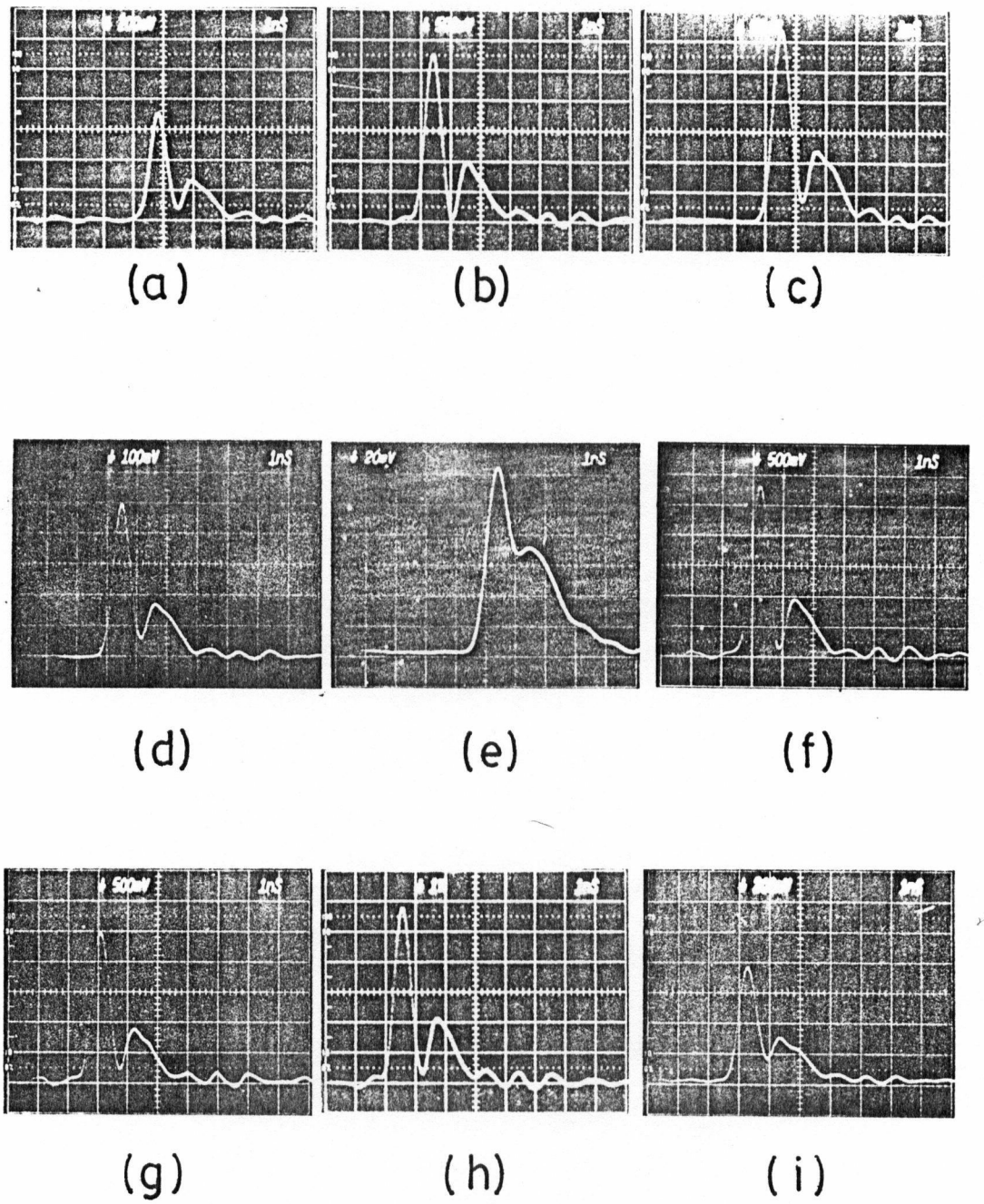

Figure 4-12 Scope traces of $(3/2)\omega_0$. In (a) $\theta = 18°$, (b) $\theta = 36°$, (c) $\theta = 54°$, (d) $\theta = 72°$, (e) $\theta = 90°$, (f) $\theta = 108°$, (g) $\theta = 126°$, (h) $\theta = 144°$, (i) $\theta = 162°$.

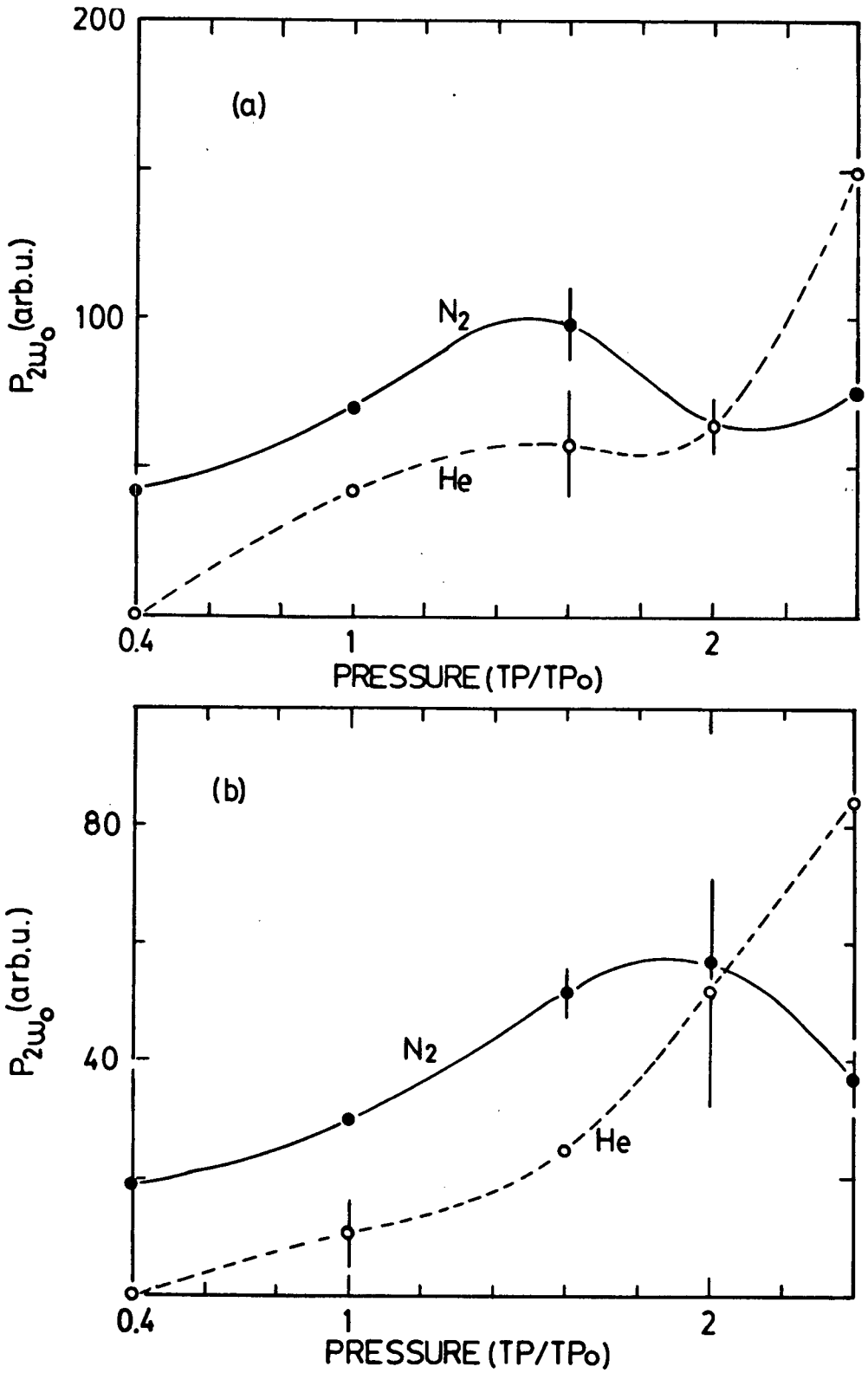

Figure 4-13 Dependence of $P_{2\omega_0}$ on the target pressure. (a) is at $\theta = 18°$ as $W_L = 6.5$J, (b) at $\theta = 18°$ as $W_L = 4.5$J, (c) at $\theta = 162°$ as $W_L = 8.5$J.

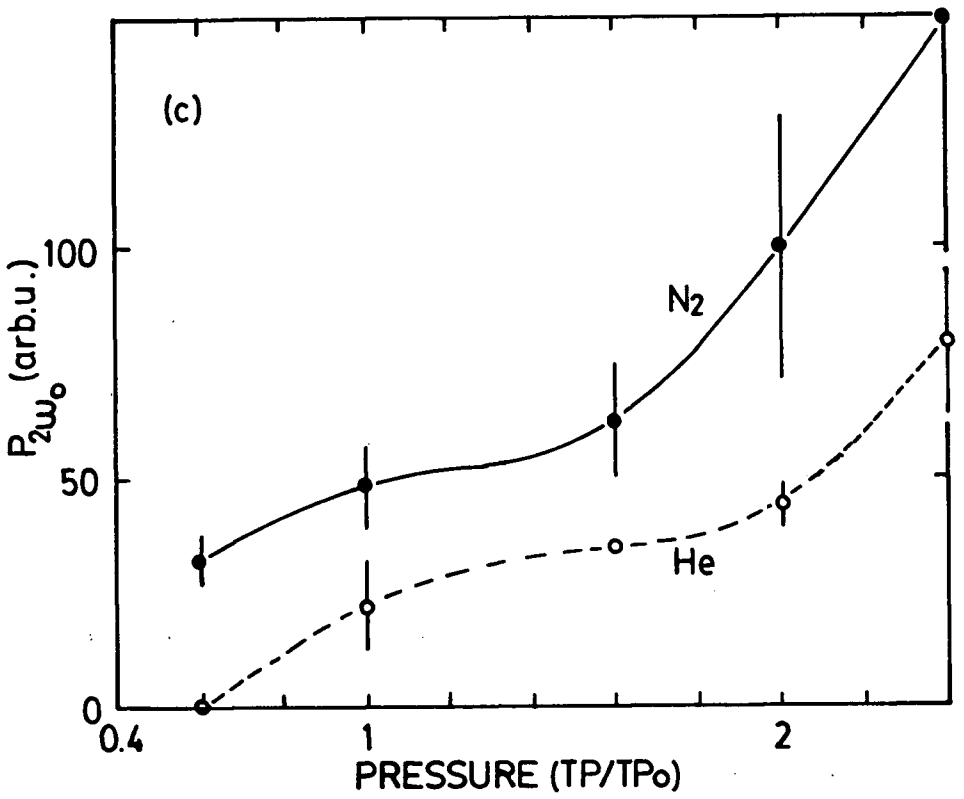

Figure 4-13 Continued.

The dependence of backward ($\theta = 162°$) emitted $(3/2)\omega_0$ radiation on the target pressure is shown in Fig. 4-14. From Fig. 4-14 one can see that for both helium and nitrogen target, when $TP/TP_0 = 0.4$, no $(3/2)\omega_0$ radiation is emitted at all. This is resonable because from ref. 46, we know as $TP/TP_0 = 0.4$, the plasma density is less than $0.25n_c$. If there is no quarter critical plasma density, no $(3/2)\omega_0$ radiation can be emitted. In the forward direction ($\theta = 18°$), for the nitrogen target, $(3/2)\omega_0$ radiation can be detected only when $TP/TP_0 = 1$; for the helium target, in a few shots $(3/2)\omega_0$-radiation is detected when $TP/TP_0 = 2.4$.

4.5 Polarization Dependence

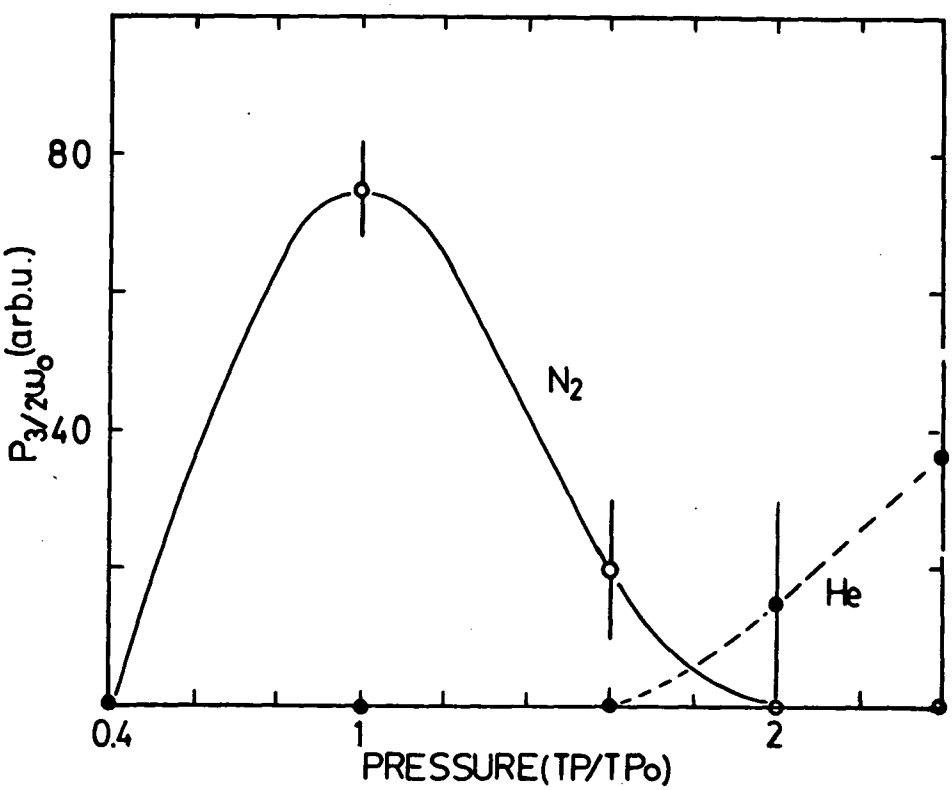

Figure 4-14 Dependence of $P_{(3/2)\omega_0}$ on the target pressure. At $\theta = 162°$ as $W_L = 6.5J$.

It was predicted in Chapter 2 that the $2\omega_0$ radiation power does not depend on the incident beam polarization. We made some measurement to prove this prediction. First we measured the harmonics in the plane of the polarization, then we meassured the harmonics in the plane perpendicular to plane of the polarization (the polarization of the laser radiation was rotated by 90° with $\lambda/2$-plate for one series of experiments). The dependence of $P_{2\omega_0}$ on the polarization of the incident laser beam is shown in Fig. 4-15 where H stands for the horizontal polarization, V for the vertical polarization. The $P_{2\omega_0}$ at $\theta = 90°$ shows dependence on the polarization as $W_L < 7.5J$ for one shot as shown in Fig. 4-15(a). Fig. 4-15(b)($\theta = 162°$) indicates that $P_{2\omega_0}$ does not depend on the polarization. Fig. 4-15(c) ($\theta =$

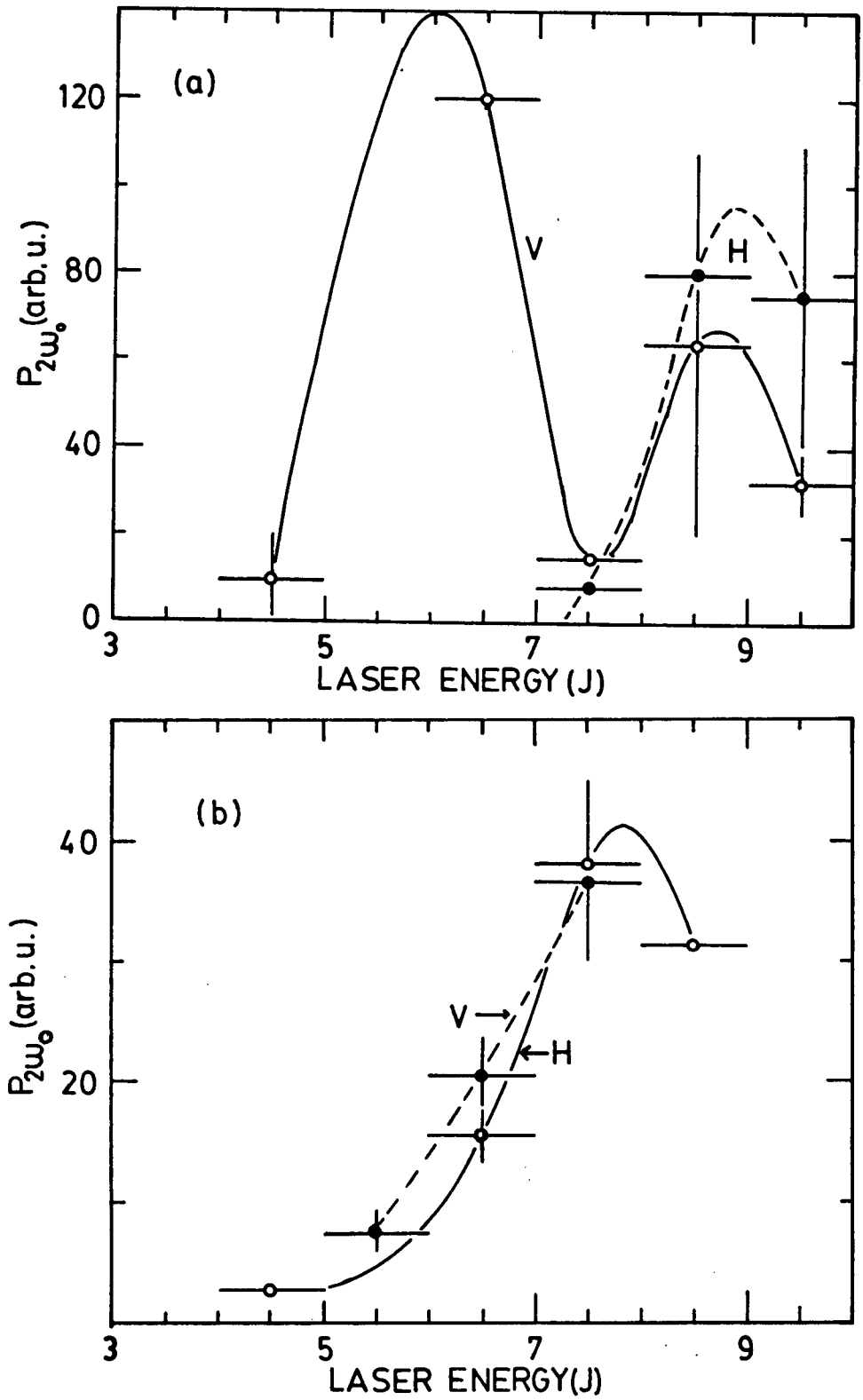

Figure 4-15 Dependence of $P_{2\omega_0}$ on the incident beam polarization. (a) is at $\theta = 90°$, (b) at $\theta = 162°$, and (c) at $\theta = 18°$.

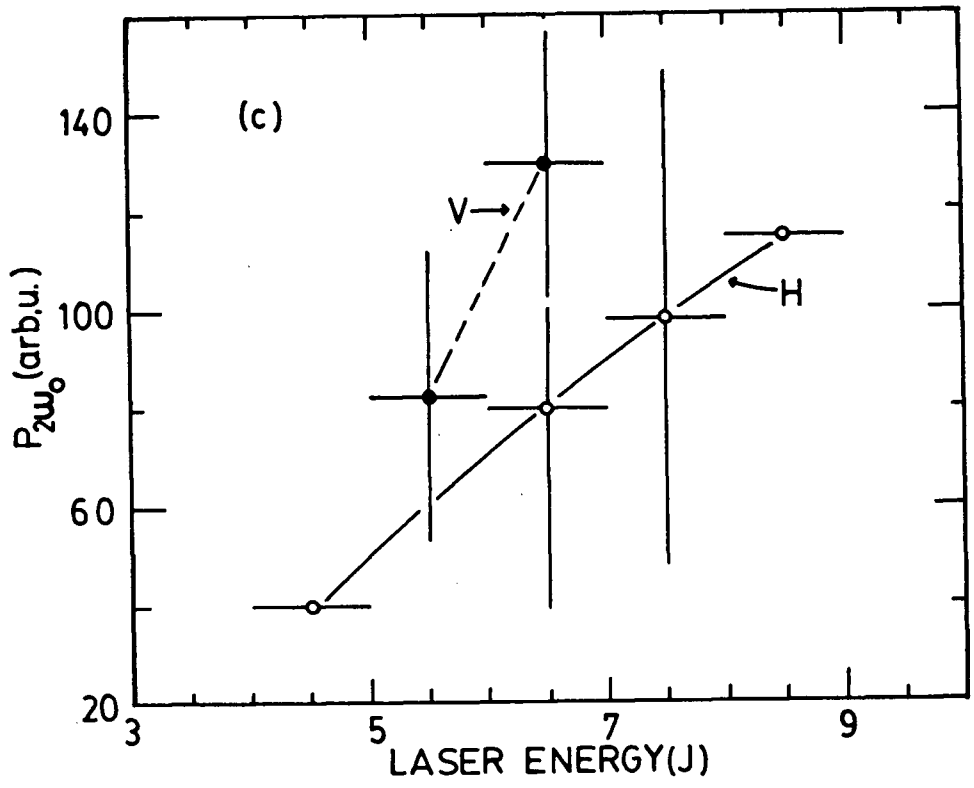

Figure 4-15 Continued.

18°) shows that $P_{2\omega_0}$ in V-polarization is stronger than in H-polarization. Therefore we can conclude that $P_{2\omega_0}$ in some directions depends on the polarization, while in some direction does not.

As shown in Fig. 4-16, we see $P_{(3/2)\omega_0}$ depends on the incident beam polarization. At $\theta = 144°$, $P_{(3/2)\omega_0}$ in the plane of the polarization of the incident beam is stronger than that in the plane perpendicular to the plane of the ploarization. While at $\theta = 90°$, the situation is just oppoite, $P_{(3/2)\omega_0}$ in the plane of the polarization is weaker than that in the plane perpendicuar to the plane of the polarization. This is not consistent with our prediction.

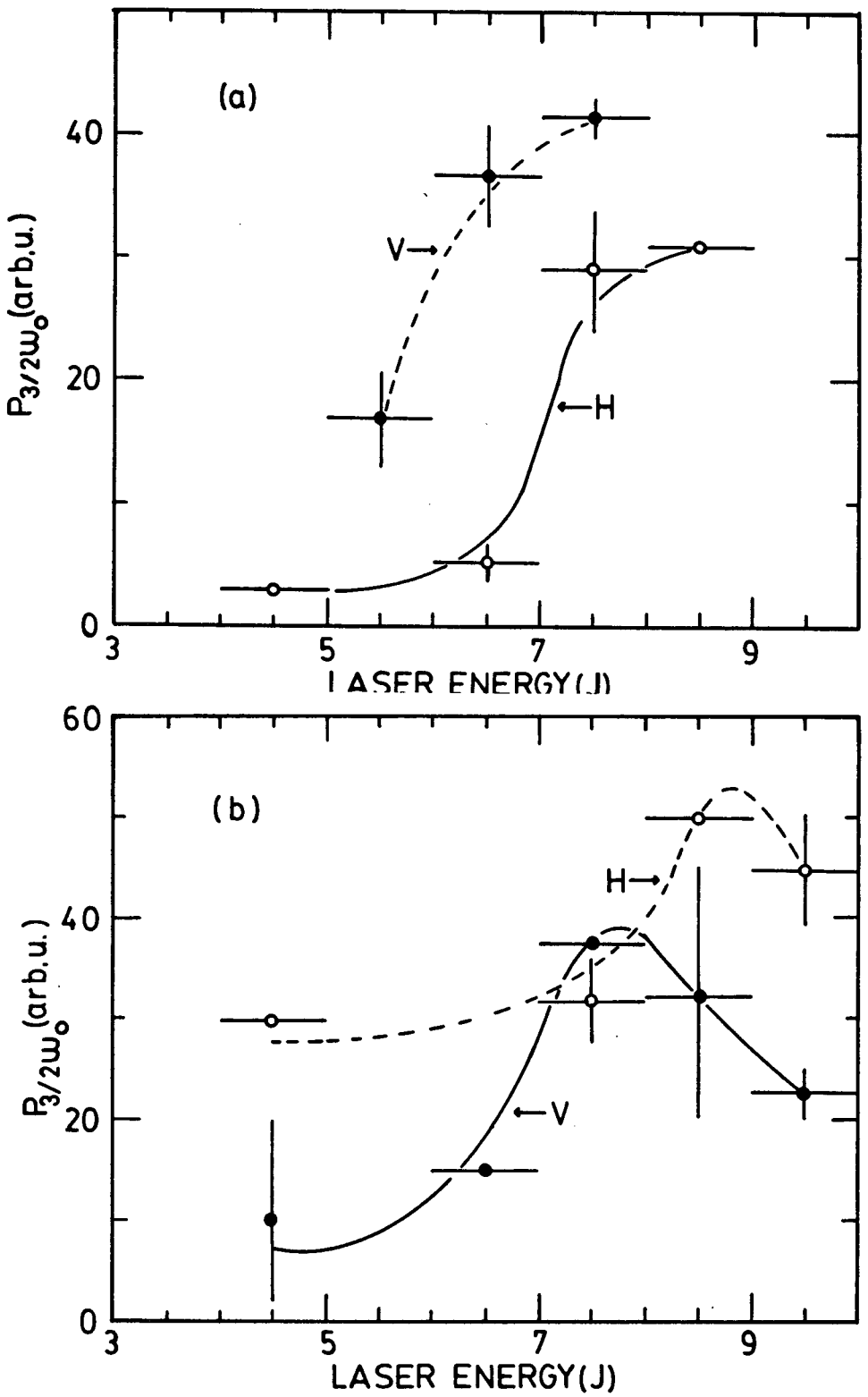

Figure 4-16 Dependence of $P_{(3/2)\omega_0}$ on the incident beam polarization. (a) is at $\theta = 90°$ and (b) at $\theta = 144°$.

CHAPTER 5

DISCUSSION OF THE RESULTS

In this chapter the detailed discussion of our experimental results is given. Evidence found from our results for our argument that the $2\omega_0$-radiation is generated by filamentation and the coupling of the incident beam with the SBS scattering are presented in Section 1. In Section 2, we try to develop a self-consistent picture for the $(3/2)\omega_0$-radiation.

5.1 $2\omega_0$-radiation

5.1.1 Filamentation contribution

The threshold power for filamentation (eq.25 of ref.42) is more than two orders of magnitude lower than the laser powers used in the present experiment and therefore self focussing is expected to occur. There is some circumstantial evidence for the presence of this instabilty. At the start of the laser pulse two breakdown plasmas are seen to form at the front and rear He-N_2 interfaces of the gas jet. Subsequently however laser energy appears to be deposited only in the front plasma indicating an inordinate amount of refraction or absorption or scattering in this region. This could be explained if the laser beam is focussed to a narrow filament in the front plasma. Late in the laser pulse axial density depressions are seen in interferograms. The axial density channel in Fig.3-2 at t = 3.3ns can be

approximated by $n_e/n_c \cong 0.13 + \rho^2/100\lambda_0^2$. Such a channel can act as a waveguide for a Gaussian laser beam with a waist $w_0 = 1.8\lambda_0$.

According to the calculations in Chapter 2 filamentation should produce a clear signature of second harmonic emission into a forward directed cone. This is indeed observed as shown in the previous chapter. The calculations are based on plane wave fronts in a constant diameter channel. Realistically however the channel diameter will be a function of z(coordinate along $\mathbf{k}_0$ and spherical wave fronts will be present in the focussing region resulting in an angular spread rather than a δ-function for the $2\omega_0$-emission as observed in Fig.4-2. The waist density is given by $n_w/n_c = \sin^2\theta_0$. The maximum at $\theta \simeq 27°$ therefore indicates $n_w = 0.2n_c$. The detected $2\omega_0$ power however is too small to be produced by a density filament of zero axial density n_0. If $n_0/n_w > 0.5$ then the density varies slowly in radial direction over the region of high intensity (see curve c in Fig.2-8) and we may use the function $H_{1,2}(x^2)$ in Fig.2-9 to estimate the $2\omega_0$ power. In order for laser radiation of 3.5J in 2ns to produce 250W of $2\omega_0$-radiation at $\theta = 27°$ as estimated from Fig.4-2 requries $H_{1,2}(x^2) = 3.3 \times 10^{-4}$. Using Fig.2-8 we find $x^2 \equiv \frac{1}{2}w_0^2k_0^2\sin^2\theta \simeq 12$ indicating a beam waist $w_0 = 1.7\lambda_0$ which is the same as that estimated from Fig.3-2 in the previous paragraph. The square law dependence of $2\omega_0$ power on incident fundamental power as suggested by eq.(2-33) is as well found experimentally(Fig. 4-4(a)). We therefore conclude that the forward emitted $2\omega_0$-radiation can be explained by the presence of plasma filaments.

5.1.2 Correlation with SBS instability

To explain the backward emitted $2\omega_0$-radiation however, the SBS instability should be considered. According to the matching conditions, there should be a backward wave with frequency around ω_0 to interact with incident beam and to generate backward emitted $2\omega_0$-radiation. One mechanism for generating such a wave is the SBS instability in the interaction of the laser with an underdense

plasma. Therefore the backward emitted $2\omega_0$ radiation could be related to the SBS instability.

Whether the backward emitted $2\omega_0$-radiation is really related to SBS instability or not can be checked by spectral measurement of the backward emitted $2\omega_0$-radiation. Since the backward emitted $2\omega_0$-radiation is generated by the coupling of the incident beam and backward SBS beam, the spectrum of backward emitted $2\omega_0$- radiation should be the same as that of backward SBS radiation. From ref. 2, we know the backward SBS radiation has $\sim 33\mathring{A}$ red shift($W_L = 7$J). This wavelength shift value agrees with our result: backward $2\omega_0$ has $\sim 40\mathring{A}$ red shift($W_L = 7.9$J). Hence, we can conclude that the backward emitted $2\omega_0$ radiation is possiblly generated by the coupling of incident beam and backward SBS radiation.

With the above conclusion, we can explain the temporal behaviour of backward emitted radiation easily as the SBS instability shows temporal behaviour[2]. The temporal behaviour of forward $2\omega_0$-radiation is hard to explain

Another possible explanation of the backward emitted $2\omega_0$-radiation is that maybe the filamentation forms a vacuum channel in the plasma, and the $2\omega_0$-radiation produced due to the filamentation links into the vacuum channel and is reflected to the backward direction.

5.1.3 Dependence on the target pressure and target material

The forward emitted $2\omega_0$-radiation is generated by filamentation. Therefore we can use eq. (2-31) to discuss the correlation of the forward emitted $2\omega_0$-radiation with the plasma density. From eq. (2-31), we see forward emitted $2\omega_0$-radiation power $P_{2\omega_0}$ is proportional to the plasma density. Therefore as the plasma density n_e increases, i.e. as the target pressure increases(the CO_2 laser beam is strong enough to fully ionize the gas in maximum target pressure which can be reached in our system), the $P_{2\omega_0}$ should increase. On other hand, from eq. (6-8)in ref. 2, we

see the SBS backscattered reflectivity relates to the plasma density by:

$$R \propto \frac{n_e^2}{n_c^2}(1 - \frac{n_e}{n_c})^{-1}. \qquad (5-1)$$

Hence as n_e increases, R increases and $E(\rho)$ in eq. (2-31) decrease, and the $P_{2\omega_0}$ decreases. Thus, the forward emitted $2\omega_0$-radiation relates to the plasma density nonlinearly with two processes. In underdense plasma, as n_e increases, the effect of filamentation is stronger than that of the reflectivity, so $P_{2\omega_0}$ increases. At some density, n_{es}, the two effects balance each other. As n_e get larger than n_{es}, the effect of reflectivity is stronger than that of the filamentation, the $P_{2\omega_0}$ decreases with plasma density.

Because the plasma density n_e is proportional to the atomic number of the target material in the same target pressure, the $P_{2\omega_0} - TP/TP_0$ curve for a helium target is moved to right with respect to the curve for a nitrogen target.

The backward emitted $2\omega_0$-radiation is generated by the coupling of the incident beam with the SBS backscattering. Backward $P_{2\omega_0}$ should increase with the plasma density since the SBS backscattering increases with the plasma density by eq. (5-1). In addition, $n_e \propto Z$, therefore $P_{2\omega_0}$ is stronger in nitrogen target than in helium target as at the same target pressure. Thus results as shown in Fig. 4-13 about density measurement are understandable. Further, the results give more evidence for the generation of $2\omega_0$-radiation by the filamentation and the coupling of the incident beam and the SBS backscattering.

5.1.4 Rotationally symmetric feature

From eq. (2-33), we know $2\omega_0$-radiation should be rotationally symmetric around the incident laser axis, and is not related to the direction of $\vec{E}_0$. Therefore the forward emitted $2\omega_0$-radiation power should not depend on the incident beam polarization. On the other hand, because of the matching conditions which govern

the coupling of the incident beam and SBS backscattering, the backward emitted $2\omega_0$-radiation power should not depend on the incident beam polarization either. Hence, we can conclude that $2\omega_0$-radiation is distributed rotationally symmetrically around laser axis, and does not depend on the incident beam polarization. This is not consistent with our observations. In some directons, $P_{2\omega_0}$ depends on the polarization as shown in Fig. 4-14.

5.2 The $(3/2)\omega_0$-radiation

5.2.1 High order nonlinear process

From ref.16 and 48, we know the threshold intensity flux for TPD instability in the interaction of CO_2 laser with the CO_2 laser-produced underdense gas jet target plasma is about $2 \times 10^{11} \mathrm{W}/cm^2$. This value is more than two orders of magnitude lower than the laser intensity flux used in our experiment. Therefore $(3/2)\omega_0$ radiation should be detected in our experiment as TPD instability occurs in the interaction.

Comparing Fig.2-3 and Fig.4-3, we see our experimental result of the angular distribution of $(3/2)\omega_0$-radiation is not consistent with the predication of Avrov's theory and Karttunen's result calculated from Liu and Resenbuth theory, and is obviously different from Baldis' result[22]. To some extent, our result agrees well with the prediction based on the wave vector matching condition with the two mechanisms. $(3/2)\omega_0$-radiation intensity peaks at $\theta = 36°$, $\theta = 72°$, $\theta = 108°$, and $\theta = 144°$: peaks at $\theta = 36°$ and $\theta = 144°$ are due to the second mechanism, peaks at $\theta = 72°$ and $\theta = 108°$ are due to the first mechanism; the peak in the backward direction is stonger than that in the forward direction for both mechanisms. Our observation as shown in Fig. 4-3 gave strong support to this prediction. And our result also shows that the angular distribution of $(3/2)\omega_0$-radiation depends on the

incident beam energy. When the incident beam energy is lower, $(3/2)\omega_0$-radiation emits evenly over a broad angular range around $\theta = 128°$, i.e. two mechanism equally contribute to the generation of $(3/2)\omega_0$-radiation. When the incident beam energy is higher, the peak at $\theta = 144°$ is stronger than that at $\theta = 108°$ and the peak at $\theta = 36°$ stronger than that at $\theta = 72°$, i.e. the second mechanism dominate the generation of $(3/2)\omega_0$-radiation. This is hard to understand since the second mechanism is a higher order nonlinear process and should be much weaker than the first mechanism. The question is raised how the higher order nonlinear process is stronger than the lower order nonlinear process.

The dependence of the angular distribution of $(3/2)\omega_0$-radiation on the incident beam energy give us some hint to this question. From ref. 7, we see the distribution of the plasma waves produced in the TPD instability in the wave vector spectrum also depends on the incident beam energy. When the incident beam energy is low, the plasma waves are almost evenly distributed in the wave vector spectrum from $k_p = 1.8k_0$ to $k_p = 4.0k_0$. When the incident beam energy is large, the most of plasma waves are distributed in the larger wave vector part of the spectrum. Most of the plasma waves are at $\theta = 45°$ and $\theta = 135°$. Now we can understand why the higher order nonlinear mechanism can be stronger than the lower order one. In the first mechanism, only the plasma waves with $\mathbf{k}_p = 1.9k_0$ can satisfy the wave vector matching condition for the scattering of incident CO_2-laser beam into $\theta = 109°$ at $(3/2)\omega_0$. In the second mechanism, the plasma waves with small and large wave vectors can satisfy the wave vector matching condition for the fusion of three plasma waves and generate $(3/2)\omega_0$-radiation. When the incident beam energy is small, since the plasma waves are almost evenly distributed in the wave vector spectrum , and in the first mechanism, the plasma waves couple with the intense incident beam to generate $(3/2)\omega_0$-radiation, both mechanisms are prevalent in the generation mechanism. While when the incident beam energy is large, the small amount of plasma waves with $k_p \sim 1.9k_0$ limits their coupling with

the incident beam. Most of the plasma waves with larger wave vector interact with each other in the second mechanism and generate $(3/2)\omega_0$-radiation. The second mechanism dominates the generation.

From the above discussion, we know that $(3/2)\omega_0$-radiation emitted at $\theta = 144°$ is due to the second mechanism. The spectrum of $(3/2)\omega_0$-radiation at $\theta = 144°$ consists of only one peak red shifted by $\Delta\bar{\lambda} = 67 \pm 35\mathring{A}$(the average is over three shots. That the average wavelenghth shift is used is because the repeatability of our system is not very high; for the same initial conditions and laser energy, we got widely varying spectra). This spectrum agrees pretty well with the estimate made in Chapter 2 with eq. (2–11). Substituting $\Delta\bar{\lambda} = 67 \pm 35\mathring{A}$, $\lambda = 10.6\mu m, \theta = 144°$ into eq. (2-11), we get $T_e = 367 \pm 191eV$. This value is close to the $T_e = 300eV$ obtained with X-ray method. If we want to use the splitting of $(3/2)\omega_0$-radiation spectrum with eq. (2-11) to estimate plasma temperature in the quarter critical plasma density region, we should improve the repeatabilty of the system with the spectrometer-image-dissector combination.

5.2.2 Dependence on the incident beam energy

The $(3/2)\omega_0$-radiation mainly emits at $\theta = 144°$ and $\theta = 36°$ when the incident beam energy is high. Here we discuss the relation between the $(3/2)\omega_0$-radiation and the laser energy only in these two directions. In other directions, since $(3/2)\omega_0$-radiation is too weak, and the measurement error is too large, the relationship is hard to discuss. From ref. 7, we know that the $(3/2)\omega_0$-radiation intensity I_s is proportional to the square of the density fluctuation amplitude δn, $I_s \propto (\delta n)^2$, and δn increases with the laser energy W_L. δn does not saturate by $W_{Lmax.} = 11J$ which is the highest energy that can be reached in our system. Hence $(3/2)\omega_0$-radiation intensity should increase with laser energy as shown in Fig. 4-6(b).

5.2.3 Correlation with target pressure and target material

The $(3/2)\omega_0$-radiation can only be generated in the laser-plasma interaction when the TPD instability occurs. If there is no quarter critical density layer in the plasma, the TPD instability cannot occur at all. From ref. 37, there is no quarter critical density layer in the plasma if $TP/TP_0 = 0.4$ for nitrogen target. Hence no $(3/2)\omega_0$-radiation is generated in the interaction as $TP/TP_0 < 0.4$. From Fig. 4-9, we can infer that there is no quarter critical density layer in the plasma as $TP/TP_0 < 1.6$ for helium target.

From ref. 24, we know that the $(3/2)\omega_0$-radiation power depends on the incident beam flux and the plasma inhomogeneity scale length a. As the target pressure TP increases, the a increases, but the SBS backscattered reflectivity also increases, i.e. the part of the incident beam interacting with quarter critical density layer decreases. Considering these two effects, whether the $(3/2)\omega_0$-radiation decreases or increases with the target pressure depends on which effect is stronger. This explanation is consistent with our results as shown in Fig. 4-14.

5.2.4 Temporal behavior of the $(3/2)\omega_0$-radiation

From Thomson scattering(Fig. 3 in ref. 7), we know that the TPD instability has two characteristic time scales due to ion-acoustic wave saturation and profile modification. The $(3/2)\omega_0$-radiation is generated in the TPD instability. Therefore the $(3/2)\omega_0$ -radiation should show two time scales. Because of the inadequate time resolution of our system, we could not asscss whether or not the TPD temporal evolution can acount for the observations.

As mentioned in Chapter 2, most of the plasma waves produced in the TPD instability propagate in opposite directions at $\sim \theta = 45^\circ$ and lie in the plane of the polarization of the incident beam. Thus, $(3/2)\omega_0$-radiation should be related to the polarization of the incident beam. This is consistent with our results as shown

in Fig. 4-15, the $(3/2)\omega_0$-radiation depends on the incident beam polarization in a complicated way.

CHAPTER 6

CONCLUSIONS AND SUGGESTIONS

In this project the second harmonic- and the three halves harmonic-radiation have been studied through the measurements of the angular distributions, spectra, dependence on the target density and target material, and dependence on the incident beam polarization.

$(3/2)\omega_0$-radiation can be generated by two mechanisms. The first is the coupling of the incident beam with a plasma wave produced in the TPD(two-plasmon decay) instability. The second is the fusion of three plasma waves produced in the TPD instability. There are three peaks in the angular distribution of the $(3/2)\omega_0$-radiation at $\theta = 36°$, $\theta = 109°$, and $\theta = 144°$ respectively. Using the matching conditions for the frequencies and vectros of the incident beam and scattered waves, it is demonstrated that the peak at $\theta = 109°$ is due to the first mechanism, while the peaks at $\theta = 36°$ and $\theta = 144°$ are due to the second mechanism. The peak in the backward direction is stronger than that in the forward direction in both mechanisms. The angular distribution of $(3/2)\omega_0$-radiation depends on the incident beam energy. When the incident beam energy, $W_L < 6$J, the both mechanisms contribute to the generation of $(3/2)\omega_0$-radiation since the plasma waves produced in TPD instability are evenly distribu ted in the wave vector spectrum from $k_p = 1.8k_0$ to $k_p = 4.0k_0$. When $W_L > 6$J, the second mechanism starts to dominate the generation of the $(3/2)\omega_0$-radiation since most of the plasma waves produced in

TPD instability occur preferentially at the larger values of k_p in the wave vector spectrum.

The spectrum of the backward emitted $(3/2)\omega_0$-radiation ($\theta = 144°$) consists of a single peak red shifted by 6.7 ± 3.5nm from $2/3\lambda_0$ and with a FWHM of 12.7nm. The red shift is consistent with that expected if the fusion of three plasma waves plays a major role in the generation fo $(3/2)\omega_0$-radiation.

If the plasma density is less than quarter critical density, the TPD instability can not occur. It is confirmed that $(3/2)\omega_0$-radiation can only be observed in the laser-plasma interaction when the TPD instability occurs. The amount of $(3/2)\omega_0$-radiation depends on the the incident beam polarization in an complicated way.

It has been commonly believed there is no $2\omega_0$-radiation generated in a laser-underdense plasma interaction. $2\omega_0$-radiation is for the first time observed in the laser-underdense plasma interaction. $2\omega_0$-radiation is mainly emitted in the forward direction($\theta = 30°$). The angular distribution of $2\omega_0$-radiation does not depend on the incident beam energy. It is thought that $2\omega_0$-radiation is generated in the laser-underdense plasma interaction by the filamentation and the coupling of the incident beam with the backward scattered wave produced by the SBS instability. The measurement of the dependence of $2\omega_0$-radiation on the target density and on the target material has given more evidence for this argument. The backscattered SBS wave intensity increases with the plasma density, the backward emitted $2\omega_0$-radation intensity also increases with the plasma density; while the forward emitted $2\omega_0$-radiation intensity in lower plasma density region, increases with the plasma density, in higher plasma desnsity region, decreases with plasma density. $2\omega_0$-radiation power is proportional to the square of the incident beam power, and is related to the incident beam polarization. A self-consistent theory about $2\omega_0$-radiation generated in the laser-underdense plasma interaction has been built.

The spectrum of forward emitted $2\omega_0$-radiation ($\theta = 18°$) is centred at $\lambda_0/2$ having a FWHM spectral width of 70Å. The spectrum of the backward emitted

$2\omega_0$-radiation($\theta = 162°$) consists a single peak red shifted by $\sim 40\mathring{A}$ and with a FWHM of $140\mathring{A}$. It is the same as that of the backscattered SBS wave.

Two original contributions have been made in this project. First, $2\omega_0$ radiation is observed for the first time in the interaction of a intense laser with a underdense plasma. Second, it has been shown that the generation of $(3/2)\omega_0$ radation can be dominated by the higher nonlinear order mechanism: the fusion of three plasma waves produced in the TPD instability.

Suggestions for the future work

The filamentation contributes to the generation of forward emitted $2\omega_0$-radiation. In order to understand $2\omega_0$-radiation thoroughly, it is essential and important to make a direct measurement of the filamentation, and to know its features. This measurement perhaps can be done with Thomson scattering.

With the matching conditions, we explained our results of the measurement of the angular distribution of the $(3/2)\omega_0$-radiation. When the second mechanism, the fusion of three plasma waves produced in the TPD instability, dominates the generation of $(3/2)\omega_0$-radiation, $(3/2)\omega_0$-radiation is emitted mainly in the directions from $\theta = 32°$ to $\theta = 45°$ and from $\theta = 135°$ to $\theta = 148°$. The plasma waves produced in the TPD istability should be a maximum in the same directions. Therefore, the direct measurement of the plasma wave angular distribution with Thomson scattering would give a strong support for this explanation. In addition, it is useful to check the $(3/2)\omega_0$-radiation polarization, to see whether the polarization depends on the incident beam polarization or not, and thereby, get more information about the mechanisms responsible for the generation of the $(3/2)\omega_0$-radiation.

When the filamentation occurs, the plasma density gradient becomes larger, and the refraction becomes stronger. It is important to study the effect of the refraction on the geometry of the generation of the harmonics.

REFERENCES

1. McCall, G.H., Plasma Phys. **25**, 237(1983).
2. Bernard, J.E., Ph.D. Thesis, University of British Columbia(1985).
3. McIntosh, G., Ph.D. Thesis, University of British Columbia(1986).
4. Legault, L., M.Sc. Thesis, University of British Columbia(1986).
5. Meyer, J., Bernard, J., Hilko, B., Houtman, H., McIntosh, G., and Popil, R., Phys. Fluids **26**, 3162(1983).
6. Meyer, J. and Houtman, H., Phys. Rev. Lett. **53**, 1344(1984).
7. Meyer, J. and Houtman, H., Phys. Fluids **28**, 1549(1985).
8. Meyer, J. and Bernard, J., Phys. Fluids **28**, 2168(1985).
9. Max, C.E. in *Laser-Plasma Interaction*, ed. I. Balian and J.C. Adam (New York, 1980), p.302.
10. Manley, J.M. and Rowe, H.E., Proc. of IRE **44**, 904(1956).
11. Ebrahim, N.A., Baldis, H.A., Joshi, C., and Benesch, R., Phys. Rev. Lett. **45**, 1179(1980).
12. Azechi, H., Ebrahim, N.A., Figueroa, H., and Joshi, C., *Ninth Conference Proceeding on Plasma Physics and Controlled Nuclear Fusion Research*(IAEA, Vinna, 1983), p.115.
13. Villeneuve, D.M., Keck, R.L., Afegan, B.B., Seka, W., and Williams, E.A., Phys. Fluids **27**, 721(1984).
14. Pant, H.C., Eidmann, K., Sachsenmaier, P., and Sigel, R., Opt. Commun.**16**, 396(1976).

15. Aleksandrov, V.V., Vikharev, V.D., Zotov, V.P., Kovalskii, N.G., and Pergament, M.I., JETP Lett. **24**, 509(1976).

16. Offenberger, A.A., Ng, A., Pitt, L., and Cervenan, M.R., Phys. Rev. **A18**, 746(1978).

17. Basov, N.G., Bychenkov, V.Yu., Zorov, N.N., Osipov, M.V., Rupasov, A.A., Silin, V.P., Sklizkov, G.V., Starodub, A.N., Tikhouchuk, V.T., and Shikanov, A.S.,m JETP Lett. **30**, 409(1978).

18. Cater, P.D., Sim, S.M.L., and Wooding, E.R., Opt. Commun. **22**, 443(1980).

19. Sim, S.M.L. and McGolkrick, E., Opt. Commun. **39**, 172(1981).

20. Turner, R.E., Phillion, D.W., Lasinski, B.F., and Campbell, E.M., Phys. Fluids **27**, 511(1984).

21. Philion, D.W., Campbell, E.M., Estabrook, K.G., Phillips, G.E., and Ze, F., Phys. Rev. Lett. **49**, 105(1982).

22. Villeneuve, D.M., Baldis, H.A., and Walsh, C.J., Phys. Fluids **28**, 1454(1985).

23. Bychenko, V.Yu., Zoxulja, A.A., Silin, V.P., and Tikhonchuk, V.K., Beitr. Plasmaphys. **23**, 331(1983).

24. Avrov, A.I., Bychenbkov, V.Yu., Krokhin, O.N., Pustovalov, V.V., Rupasor, A.A., Silin, V.P., Sklizkov, G.V., Tikhonchuk, V.T., and Shikanov, A.S., JETP **45**, 507(1977).

25. Liu, C.S. andf Rosenbluth, M.N., Phys. Fluids **19**, 967(1976).

26. Baldis, H.A. and Walsh, C.J., Phys. Fluids **26**, 1364(1983).

27. Aboites, V., Hughes, T.P., McGoldrick, E., Sim, S.M.L., Karttunen, S.J., and Evans, R.G., Phys. Fluids **28**, 2555(1985).

28. Jackel, S., Perry, B., and Lubin, M., Phys. Rev. Lett. **37**, 95(1976).

29. Powers, L.V. and Schroeder, R.J. (private communication).

30. McGoldrick, E. and Sim, S.M.L., Opt. Commun. **39**, 3(1981).

31. Cater, P.D., Sim, S.M.L., Barr, H.C., and Evans, R.G., Phys.Rev. Lett. **44**, 21(1980).

32. Barr, H.C., *Science Research Council Laser Facility Annual Report* No. RL-79-036, p.8.12.

33. Karttunen, S.J., (private communication).

34. Meyer, J., Bernard, J.E., Hilko, B., Houtman, H., McIntosh, G., Popil, R., Phys. Rev. **A29**, 1375(1984).

35. Carman, R.L., Rhodes, C.K., and Benjamin, R.F., Phys. Rev. Lett. **A24**, 2649(1981).

36. Burnett, N.H., Baldis, H.A., Richardson, M.C., and Enright, G., Appl. Phys. Lett. **31**, 172(1977).

37. McLean, E.A., Stamper, J.A., Ripin, B.H., McMahon, J.M., and Bodner, S.E., Appl. Phys. Lett. **31**, 825(1977).

38. Stamper, J.A., Lehmburg, R.H., Schmitt, A., Herbst, M.J., Young, F.C., Gardner, J.H., and Obenschain, S.P., Phys. Fluids **28**, 2563(1985).

39. Shen, Y.R., *The Principles of Nonlinear Optics*, J.Wiley & Sons, (New York, 1984), p.8-11.

40. Jackson, J.D., *Classical Electrodynamics* J.Wiley & Sons, (New York· London, 1962), p.468.

41. Gradshteyn, I.S. and Ryzhik, I.M., *Table of Integrals, Series, and Products*, (Academic Press, New York, 1980), p.716 and p.1058, 1059.

42. Kaw, P., Schmidt, G., and Wilcox, T., Phys. Fluids **16**, 1522(1973).

43. Sodha, M.S., Ghatak, A.K., and Tripathi, V.K., *Progress in Optics XIII*, ed. Wolf, E., (North Holland, Amsterdam, 1976), p.169.

44. Kogelnik, H., Appl. Opt. **4**,1562(1965).

45. Popil, R., Ph.D. Thesis, University of British Columbia (1984).

46. McIntosh, G., Master Thesis, University of British Columbia(1983).

47. Baldis, H.A., Burnett, N.H., and Richardson. M.C., Rev. Sci. Instrum. **48**, 173(1977).

48. Rosenbluth, M.N., Phys. Rev. Lett. **29**, 565(1972).